Cosmogenic 10Be in pyroxene: laboratory progress, production rate systematics, and application of the 10Be-3He nuclide pair in the Antarctic Dry Valleys

Allie Balter-Kennedy, Joerg M. Schaefer, Roseanne Schwartz, Jennifer L. Lamp, Laura Penrose, Jennifer Middleton, Jean Hanley, Bouchaïb Tibari, Pierre-Henri Blard, Gisela Winckler, et al.

Geochronology, 5, 301–321, 2023
https://doi.org/10.5194/gchron-5-301-2023

Cosmogenic ^{10}Be in pyroxene: laboratory progress, production rate systematics, and application of the ^{10}Be–^{3}He nuclide pair in the Antarctic Dry Valleys

Allie Balter-Kennedy[1,2], Joerg M. Schaefer[1,2], Roseanne Schwartz[1], Jennifer L. Lamp[1], Laura Penrose[1], Jennifer Middleton[1], Jean Hanley[1], Bouchaïb Tibari[3], Pierre-Henri Blard[3], Gisela Winckler[1,2], Alan J. Hidy[4], and Greg Balco[5]

[1]Lamont–Doherty Earth Observatory, Columbia University, Palisades, NY 10964, USA
[2]Department of Earth and Environmental Sciences, Columbia University, New York, NY 10027, USA
[3]CRPG, CNRS, Université de Lorraine, 54 000 Nancy, France
[4]Department is Center for Accelerator Mass Spectrometry, Lawrence Livermore National Laboratory, Livermore, CA 94550, USA
[5]Berkeley Geochronology Center, Berkeley, CA 94709, USA

Correspondence: Allie Balter-Kennedy (abalter@ldeo.columbia.edu)

Received: 1 December 2022 – Discussion started: 21 December 2022
Accepted: 11 May 2023 – Published: 17 July 2023

Abstract. Here, we present cosmogenic-^{10}Be and cosmogenic-^{3}He data from Ferrar dolerite pyroxenes in surficial rock samples and a bedrock core from the McMurdo Dry Valleys, Antarctica, with the goal of refining the laboratory methods for extracting beryllium from pyroxene, further estimating the ^{10}Be production rate in pyroxene and demonstrating the applicability of ^{10}Be–^{3}He in mafic rock. The ability to routinely measure cosmogenic ^{10}Be in pyroxene will open new opportunities for quantifying exposure durations and Earth surface processes in mafic rocks. We describe scalable laboratory methods for isolating beryllium from pyroxene, which include a simple hydrofluoric acid leaching procedure for removing meteoric ^{10}Be and the addition of a pH 8 precipitation step to reduce the cation load prior to ion exchange chromatography. ^{10}Be measurements in pyroxene from the surface samples have apparent ^{3}He exposure ages of 1–6 Myr. We estimate a spallation production rate for ^{10}Be in pyroxene, referenced to ^{3}He, of 3.6 ± 0.2 atoms g^{-1} yr^{-1}. ^{10}Be and ^{3}He measurements in the bedrock core yield initial estimates for parameters associated with ^{10}Be and ^{3}He production by negative-muon capture ($f_{10}^{*} = 0.00183$ and $f_{3}^{*} f_{\mathrm{C}} f_{\mathrm{D}} = 0.00337$).

Next, we demonstrate that the ^{10}Be–^{3}He pair in pyroxene can be used to simultaneously resolve erosion rates and exposure ages, finding that the measured cosmogenic-nuclide concentrations in our surface samples are best explained by 2–8 Myr of exposure at erosion rates of 0–35 cm Myr^{-1}. Finally, given the low ^{10}Be in our laboratory blanks (average of 5.7×10^{3} atoms), the reported measurement precision, and our estimated production rate, it should be possible to measure 2 g samples with ^{10}Be concentrations of 6×10^{4} and 1.5×10^{4} atoms g^{-1} with 5 % and 15 % uncertainty, respectively. With this level of precision, Last Glacial Maximum to Late Holocene surfaces can now be dated with ^{10}Be in pyroxene. Application of ^{10}Be in pyroxene, alone or in combination with ^{3}He, will expand possibilities for investigating glacial histories and landscape change in mafic rock.

1 Introduction

Cosmogenic nuclides are formed in minerals when rock is exposed to secondary cosmic radiation, and their concentrations at and near the Earth's surface hold information about exposure durations, burial time, and erosion rates (e.g., Cerling, 1994; Kurz and Brook, 1994; Lal, 1991; Nishiizumi et al., 1991; Schaefer et al., 2022). Most simply, the concentration of cosmogenic nuclides in rock serves as an ex-

posure clock because they accumulate at known rates. It is also possible to deconvolve complex exposure histories, involving exposure, burial, and rock erosion, by combining measurements of multiple cosmogenic nuclides with different half-lives (e.g., Balco and Rovey, 2010; Granger, 2006; Lal, 1991; Nishiizumi et al., 1991; Schaefer et al., 2016a). In quartz-bearing (felsic) rocks, ^{21}Ne (stable), ^{10}Be ($t_{1/2} =$ 1.4 Myr), ^{26}Al ($t_{1/2} = 0.7$ Myr), and ^{14}C ($t_{1/2} = 5.7$ kyr) are routinely measured, and different combinations of these nuclides can be used to quantify geomorphic processes on 10^3–10^6-year timescales (e.g., Balco and Shuster, 2009; Hippe, 2017; Young et al., 2021). ^{10}Be in quartz is the most commonly used nuclide–mineral pair because this mineral phase is abundant at the Earth's surface, the production pathways for ^{10}Be in quartz are well understood, and advances in beryllium extraction procedures and mass spectrometry have yielded measurement precision as low as ~ 2 %.

Fewer cosmogenic nuclides are routinely measured in lithologies where quartz is absent. The stable nuclide ^{3}He is the most widely used in mafic rocks because it is easily measured in several mineral phases, including pyroxene and olivine (Blard et al., 2021; Kurz, 1986). The radionuclide ^{36}Cl ($t_{1/2} = 0.3$ Myr) is also routinely measured in feldspar or whole rock, so the ^{36}Cl–^{3}He pair could in principle be used to detect burial up to ~ 1.5 Ma. Prior work demonstrates that measuring ^{10}Be in pyroxene and olivine is possible (Blard et al., 2008; Eaves et al., 2018; Ivy-Ochs et al., 1998; Nishiizumi et al., 1990), which would extend the useful range for multi-nuclide studies in mafic rocks to > 5 Ma, ideal for Miocene to Pleistocene timescales.

Several studies report ^{10}Be concentrations in pyroxene (Blard et al., 2008; Eaves et al., 2018; Ivy-Ochs et al., 1998) but highlight challenges to measuring ^{10}Be in this mineral phase. First, the mineral composition of pyroxene ($XYSi_2O_6$, where X and Y are both divalent cations (primarily Ca, Fe, or Mg), or X is a monovalent cation (Na, Li), and Y is a trivalent cation (Al, Fe); Nespolo, 2020)) is highly variable. In contrast to quartz (SiO_2), the high cation quantities in pyroxenes present a significant challenge for isolating beryllium using ion exchange chromatography, limiting the feasible sample size. Second, early work on pyroxenes demonstrated difficulty in removing meteoric ^{10}Be, atmospherically produced ^{10}Be scavenged by precipitation. In quartz, meteoric ^{10}Be is typically removed by repeated leaching in hydrofluoric acid (HF; Brown et al., 1991; Kohl and Nishiizumi, 1992). Ivy-Ochs et al. (1998) demonstrated that ^{10}Be concentrations in pyroxenes with exposure ages of $\sim 10^6$ years did not stabilize after several rounds of HF leaching, suggesting that meteoric ^{10}Be was present in clays and other weathering products built up within the pyroxene lattice. In samples with 10^4-year exposure ages, Blard et al. (2008) successfully decontaminated pyroxene of meteoric ^{10}Be by implementing a powdering step to increase the surface area of pyroxene grains prior to leaching the samples in hydroxylammonium chloride, which removes iron oxides and releases meteoric ^{10}Be from the pyroxene grains. This result was replicated by Eaves et al. (2018), but this procedure has yet to be tested on pyroxenes with exposure durations longer than 10^4 years, in which weathering products have had more time to accumulate within the pyroxene lattice.

For cosmic-ray-produced nuclides to be useful in geologic applications, the production rate of these nuclides at the Earth's surface and with depth in rock must be known. ^{10}Be and ^{3}He, like most cosmogenic nuclides, are produced by spallation, fast-muon interactions, and negative-muon capture, production pathways that display different dependencies (Dunai, 2010). Spallation reactions, induced by high-energy (30 MeV–1 GeV) neutrons, comprise the majority of production at the Earth's surface but decrease rapidly with depth due to strong interaction with matter, with a latitude-dependent attenuation length in rock of 140–160 g cm^{-2} (Gosse and Phillips, 2001). Production by muons, which interact weakly with matter, comprise up to ~ 2 % of production at the surface but surpass spallation production below the upper several meters of rock. For this weak interaction production pathway, ^{10}Be and ^{3}He are primarily produced by negative-muon capture in the upper rock column, while fast-muon reactions attenuate more slowly with depth from the surface (Balco, 2017; Heisinger et al., 2002a, b; Lal, 1987; Larsen et al., 2021; Nesterenok and Yakubovich, 2016).

The spallation production rate of ^{3}He in pyroxene is well known (Borchers et al., 2016; Goehring et al., 2010). Eaves et al. (2018) used cross-calibration between ^{10}Be and ^{3}He (combining new data with those of Blard et al., 2008, and Nishiizumi, 1990) to estimate a spallation ^{10}Be production rate in pyroxene of 3.6 ± 0.8 atoms g^{-1} yr^{-1} (Eaves et al., 2018, also calibrated a production rate for ^{10}Be in pyroxene of 3.2 ± 0.8 atoms g^{-1} yr^{-1} using independent age data). Theoretical studies predict that cosmogenic ^{3}He is produced by muon interactions (Lal, 1987; Nesterenok and Yakubovich, 2016), and recent ^{3}He measurements in a 300 m drill core from the Columbia River Basalt provide unambiguous empirical evidence for muon production of ^{3}He at a total production rate of 0.23–0.45 atoms g^{-1} yr^{-1} at the Earth's surface at sea level high-latitude (Larsen et al., 2021). Although parameters associated with muon production of ^{10}Be in quartz are well known (Balco, 2017), muon production of ^{10}Be in pyroxene is not yet quantified.

Here, we describe progress in laboratory techniques for extracting beryllium from pyroxene, building upon the previous work of Blard et al. (2008) and Eaves et al. (2018). We then use our new ^{10}Be and ^{3}He measurements in pyroxenes from surface samples and a 1.7 m drill core from the McMurdo Dry Valleys, Antarctica, to further calibrate the production rate of ^{10}Be by spallation and present initial constraints on ^{10}Be and ^{3}He production by negative-muon capture. Finally, we use the sample set from the McMurdo Dry Valleys to demonstrate use of the ^{10}Be–^{3}He pair for simultaneously estimating exposure ages and erosion rates in mafic rock.

2 Geologic setting

The McMurdo Dry Valleys region of Antarctica is a 4800 km^2 area in the northern Transantarctic Mountains, bounded by the McMurdo Sound to the west and the East Antarctic Ice Sheet (EAIS) to the east. Local basement rock and overlying sedimentary rocks are intruded by Jurassic Ferrar dolerite sills (∼ 180 Ma; Burgess et al., 2015; McKelvey and Webb, 1962). The landscape is dissected by the large, east–west trending Taylor, Wright, and Victoria Valley systems that formerly held outlet glaciers draining the EAIS to the Ross Sea and are flanked by mountains, including the Asgard and Olympus ranges (Fig. 1). Geomorphic evidence suggests that this landscape had formed by the mid-Miocene and has since been preserved in a cold, hyperarid climate (e.g., Sugden et al., 1995). This hypothesis is supported by extremely high cosmogenic-nuclide concentrations throughout the region that are consistent with some of the lowest subaerial erosion rates on Earth (0–30 cm Myr^{-1}; Bruno et al., 1997; Ivy-Ochs et al., 1995; Margerison et al., 2005; Schäfer et al., 1999; Summerfield et al., 1999).

Large meltwater features, including channels, potholes, plunge pools, corrugated bedrock, and megaripples, found throughout the region are thought to have been carved by mid-Miocene outburst floods originating beneath an expanded, wet-based EAIS (Denton and Sugden, 2005). ^{40}Ar / ^{39}Ar ages of in situ volcanic ashes embedded in associated sediments provide limiting ages of these features, suggesting that the major topographic features of the Dry Valleys formed by ∼ 15 Ma and that the last glacial overriding event likely occurred by 14 Ma and possibly by 14.8 Ma (Denton et al., 1993). One prominent meltwater feature is the Labyrinth, a channel-and-pothole system carved into Ferrar dolerite bedrock located at the foot of Wright Upper Glacier, an outlet glacier of the EAIS. ^{39}Ar / ^{40}Ar ages of ashes from erosional surfaces within the Labyrinth date the last incision of this feature to ∼ 14.5 Ma (Lewis et al., 2006). In contrast, cosmogenic-nuclide concentrations in similar sandstone channel systems in Sessrumnir Valley, Asgard Range, near, although not directly adjacent to, the Labyrinth suggest that the Dry Valleys landscape has been more dynamic since the mid-Miocene. There, paired ^{10}Be–^{21}Ne data reveal lower-than-expected cosmogenic-nuclide concentrations, which can be explained if these features had formed by wind erosion since ∼ 14 Ma at erosion rates of ∼ 60–150 cm Myr^{-1} or were incised by subglacial flooding during a later episode of ice cover, such as during the Pliocene (Middleton et al., 2012). Overall, channel and pothole features throughout the Dry Valleys, including the Labyrinth, may have experienced ∼ 14–15 Myr of exposure, although the mechanism and timing of formation for many of these features remain up for debate.

In this study, we focus on Ferrar dolerite samples collected throughout the Dry Valleys region, originally measured for cosmogenic noble gasses by Bruno et al. (1997) and Schaefer et al. (1999), that can be grouped into two geomorphic environments: (1) boulders that are erosional remnants of the Sirius Group, located atop Mt. Fleming and Mt. Feather at elevations > 2000 m in the Stable Upland Zone, which features the coldest and driest conditions in the Dry Valleys (Lamp et al., 2017, and references therein), and (2) bedrock collected between ∼ 850–1400 m from deeply weathered platforms at Mt. Insel, the Dais, and the Labyrinth in the inner Dry Valleys, somewhat closer to the Ross Sea, where conditions are slightly warmer and wetter (see Schäfer et al., 1999, and Bruno et al., 1997, for further details; Fig. 1). In addition to surface samples, we include results from a bedrock core collected from an erosional surface of the Labyrinth.

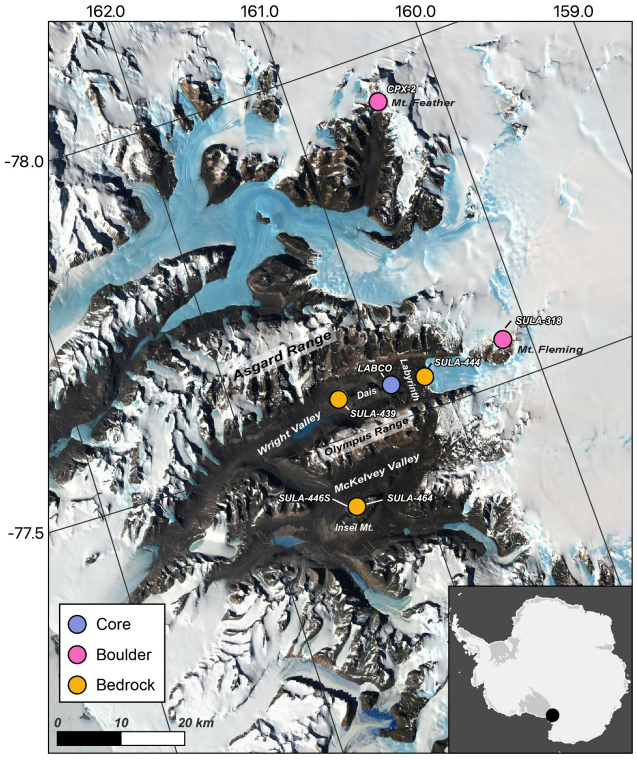

Figure 1. Map showing sample locations and places discussed in the text generated using Quantarctica Version 3 (Matsuoka et al., 2021). The base map employs the LIMA Landsat high-resolution virtual mosaic (Bindschadler et al., 2008).

3 Methods

3.1 Field methods

We present results from surficial rock samples and a bedrock core. The surficial rock samples are six Ferrar dolerites collected from the upper few centimeters of rock in the Dry Valleys in the early to mid-1990s and described by Schäfer et al. (1999) and Bruno et al. (1997) (two boulders and four bedrock surfaces; Table 1). We redetermined surface sample locations and elevations with reference to the US Geologi-

Table 1. Location information for surface samples.

Sample ID	Location	Sample type	Latitude[c] (decimal degrees)	Longitude[c] (decimal degrees)	Elevation (m)	Thickness (cm)	Shielding
318[a]	Mt. Fleming	Boulder	−77.56	160.17	2140	1.5	1
439	Dais	Bedrock	−77.56	161.31	870	1.5	1
446S	Mt. Insel	Bedrock	−77.40	161.43	1410[d]	1.5	1
464	Mt. Insel	Bedrock	−77.40	161.42	1395[d]	1.5	1
NXP 93*52[b]	Mt. Feather	Boulder	−77.93	160.42	2555	1.5	1
444	Labyrinth	Bedrock	−77.55	160.74	1145	1.5	1
Labyrinth core	Labyrinth	Core top	−77.54976	160.9578	990.2	1	1

[a] Sample is listed as Flem94-18 in Bruno et al. (1997) and is the only sample listed here included in that publication. [b] Sample NXP 93*52 is derived from the same sample as the reference material CRONUS-P (Schaefer et al., 2016b). [c] Latitudes and longitudes for surface samples are approximated from the United States Geological Survey (1988) Taylor Glacier map, as latitudes and longitudes were not reported in the original publications associated with these samples (Bruno et al., 1997; Schäfer et al., 1999). See Supplement for location approximation methods. [d] Sample elevations used here are 120 m lower than reported in Schäfer et al. (1999) due to inaccuracies with pressure-based altimeter/early handheld GPS. See Supplement.

cal Survey Taylor Glacier topographic map (1988) because of some inaccuracies with the location information in those original publications (see Table S1 in the Supplement). The Labyrinth bedrock core was collected by a group led by John Stone of the University of Washington in austral summer 2009 as part of the CRONUS-Earth project (Table 1, Fig. 1, Sect. 2). The rock type is fine- to medium-grained Ferrar dolerite, with roughly equal parts of pyroxene and plagioclase. The coring site was chosen because erosion rates appeared to be low (10–20 cm Myr^{-1}), and previous work suggests that the site has been exposed for the last $\sim$ 14 Myr (Lewis et al., 2006; Sect. 2). Importantly, below 18 cm depth, there was a discrepancy between the drillers' measurements of the core barrel and the recovered core length by 1–4 cm. No material was lost between 18–167 cm, but we account for this discrepancy by adjusting the absolute sample depths below 18 cm in a model fitting exercise described in Sect. 5.1.1. The core was split into sections at the University of Washington and measured for rock density. Four rock density measurements from 0.5–1.5 m depth in the core gave consistent values from 2.93 ± 0.02 to 2.96 ± 0.02 g cm^{-3}, averaging 2.94 ± 0.03 g cm^{-3}. Sections of the core were then sent to several institutions, including Lamont–Doherty Earth Observatory (LDEO), Berkeley Geochronology Center (BGC), and Le Centre de Recherches Pétrographiques et Géochimiques (CRPG), for cosmogenic-nuclide analysis.

3.2 Cosmogenic-nuclide measurements

3.2.1 Mineral separation and decontamination

Pyroxene separated from the surface samples was prepared at LDEO, and samples from the Labyrinth core were prepared at LDEO, BGC, and CRPG. At LDEO, samples were crushed and sieved to a grain size at which we observed mostly mono-mineralic grains (for the fine- to medium-grained samples here, we used the 32–125 µm fraction) and then leached at room temperature in 10 % H_3PO_4 overnight to remove iron oxides. Then light minerals (mostly plagioclase) were removed using sodium polytungstate with a density of 3.0 g cm^{-3}. Next, samples were passed through a magnetic separator, and a hand magnet was used to remove magnetic minerals. To decontaminate the pyroxene grains of meteoric ^{10}Be, samples were leached in a 1 %HF / 1 %HNO_3 solution and placed on a table shaker at room temperature for 5–6 h twice, then a third time overnight, rinsing samples thoroughly between each round of leaching (Bromley et al., 2014; Kohl and Nishiizumi, 1992). Overall, we targeted $\sim$ 30 % sample mass loss after leaching. To confirm sufficient removal of meteoric ^{10}Be, five leaching rounds were performed on sample 444, and the ^{10}Be concentration was measured on a split taken after each round. After two rounds of leaching, with $\sim$ 25 % sample loss, ^{10}Be concentrations in sample 444 remain consistent within measurement error, suggesting that this leaching method was sufficient for removing meteoric ^{10}Be (Fig. 2). Pyroxenes separated at LDEO are referred to as "LDEO-prepared."

Pyroxene preparation procedures at BGC and CRPG, where pyroxenes were measured only for ^{3}He, were similar to those at LDEO but did not include an HF leaching step. BGC received from the University of Washington a heavy mineral concentrate prepared by crushing, sieving to extract grains in the 125–250 µm size range, and heavy liquid separation at 2.9 g cm^{-3}. This concentrate was then repeatedly passed through a magnetic separator at various settings to separate pure pyroxene from pyroxene–plagioclase aggregates (less magnetic) and oxide minerals (more magnetic). Remaining contaminant grains were then removed by handpicking under a microscope. At CRPG, samples were crushed and sieved to 150–800 µm, plagioclase was removed by heavy liquid separation at a density of 3.3 g cm^{-3}, and then samples underwent magnetic separation and handpicking to improve the selection of pure pyroxenes. Based on inductively coupled plasma optical emission spectroscopy

Table 2. Cosmogenic-nuclide concentrations, apparent exposure ages, and apparent erosion rates for surface samples.

Sample ID	Location	Measured $[^3He]^d$ (atoms g^{-1})	$[^3He]$ normalized to CRONUS-P[d] (atoms g^{-1})	$[^3He]$ error[d] (atoms g^{-1})	Measured $[^{10}Be]$ (atoms g^{-1})	$[^{10}Be]$ error (atoms g^{-1})	Apparent ^3He exposure age (years)	Apparent exposure ^3He age error (years)	Apparent ^{10}Be exposure age[e] (years)	Apparent ^{10}Be exposure age error (years)	$^{10}Be/^3He$ age ratio	Apparent ^3He erosion rate (cm Myr^{-1})	Apparent ^3He erosion rate error (cm Myr^{-1})
318[a]	Mt. Fleming	6.09E+09	5.87E+09	1.50E+08	5.06E+07	1.21E+06	6.25E+06	1.54E+05	4.39E+06	3.82E+05	0.70	8.7	0.2
439	Dais	9.20E+08	8.86E+08	2.00E+07	1.55E+07	3.72E+05	2.58E+06	5.62E+04	2.71E+06	1.38E+05	1.05	21.1	0.5
446S	Mt. Insel	3.08E+09	2.97E+09	8.00E+07	2.84E+07	6.80E+05	5.47E+06	1.42E+05	3.97E+06	3.00E+05	0.72	10.0	0.3
464	Mt. Insel	2.78E+09	2.68E+09	7.00E+07	2.75E+07	6.57E+05	5.00E+06	1.26E+05	3.73E+06	2.61E+05	0.75	10.9	0.3
NXP 93*52[b]	Mt. Feather	5.21E+09	5.02E+09	2.50E+08	6.46E+07	1.54E+06	4.04E+06	1.94E+05	3.91E+06	2.89E+05	0.97	13.5	0.7
444	Labyrinth	5.20E+08	5.01E+08	2.00E+07	1.02E+07	2.46E+05	1.15E+06	4.42E+04	9.72E+05	3.02E+04	0.85	47.3	0.2
Labyrinth core[c]	Labyrinth	4.54E+08	4.77E+08	9.23E+06	–	–	1.24E+06	2.53E+04	8.25E+05	1.53E+04	0.66	43.8	0.9

[a] Sample is listed as Flem94-18 in Bruno et al. (1997) and is the only sample listed here that is included in that publication. [b] Sample NXP 93*52 is derived from the same sample as the reference material CRONUS-P (Schaefer et al., 2016b). [c] ^3He concentrations listed here are for the only surface sample in which ^{10}Be was not measured. See Table 3 for subsurface sample results. To calculate the ^{10}Be surface exposure age, a surface ^{10}Be concentration was approximated by fitting an exponential curve to the subsurface ^{10}Be data. [d] ^3He concentrations reported for all samples except the Labyrinth core were measured at LDEO and were originally reported in Schaefer et al. (2006). [e] Apparent ^{10}Be exposure ages calculated using the ^{10}Be in pyroxene spallation production rate from Eaves et al. (2018) of 3.6 ± 0.8 atoms g^{-1} yr^{-1} and v3 of the online exposure age calculator.

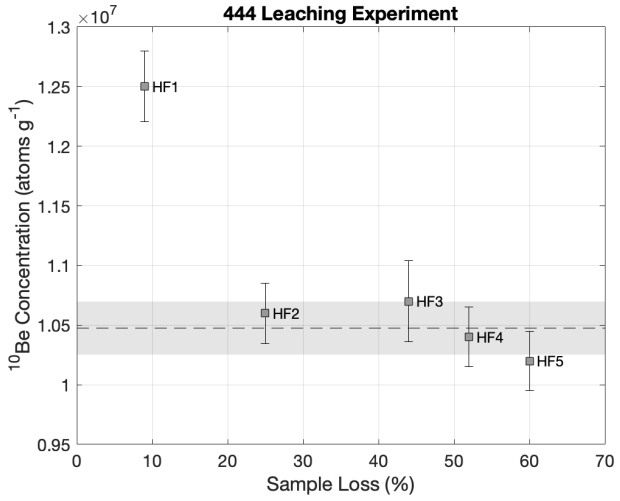

Figure 2. ^{10}Be concentrations measured after each of the five progressive leaches on pyroxenes from sample 444. Total sample material loss ranges from 9 % in Leach 1 to 60 % in Leach 5. The dashed black line shows the average ^{10}Be concentration of HF2–HF5, and the shaded box shows the standard deviation of those ^{10}Be concentrations. The HF2–HF5 concentrations overlap within uncertainty, suggesting that 20 %–25 % sample loss is enough to sufficiently remove meteoric ^{10}Be from old Ferrar dolerite samples.

(ICP-OES) data (Tables S1 and S2), analyzed pyroxene separates were primarily clinopyroxene (augite).

3.2.2 Cosmogenic-^{3}He analyses

^{3}He concentrations in the Labyrinth bedrock core samples were measured at LDEO, BGC, and CRPG. For quality control, internal comparability, and interlaboratory calibration, we also measured helium isotopes in the CRONUS-P pyroxene reference material, which is derived from the NXP 93*52 surface sample (Blard et al., 2015; Schaefer et al., 2016b; Table 2). For all samples, we normalize the measured ^{3}He concentrations to the accepted CRONUS-P value ($(5.02 \pm 0.05) \times 10^9$ atoms g^{-1}; Tables 1 and 2; Blard, 2021; Blard et al., 2015). At all laboratories, relative measurement uncertainties for the Labyrinth core samples increased with depth owing to the decreasing ^{3}He concentrations, ranging from 2 % in the uppermost sample to 4 % in the lowermost sample.

At LDEO, we measured helium isotopes in eight LDEO-prepared Labyrinth core samples. We extracted helium in two subsequent heating steps, 5 min at ∼ 900 °C and 15 min at 1350 °C in a resistance-heated double-vacuum furnace. Following purification with a charcoal-filled, liquid-nitrogen-cooled U trap and SEAS getter, the gas was cryo-trapped at 14 °C. The helium fraction was released at 45 °C, and ^{3}He and ^{4}He were measured by peak jumping in a MAP 215-50 (e.g., Winckler et al., 2005). Spectrometer sensitivity was determined using a Yellowstone helium standard (Mur-

dering Mudpots) with a $^3He/^4He$ ratio of $16.45R_a$ (where $R_a = (^3He/^4He)_{air} = 1.384 \times 10^{-6}$). Blank corrections were $< 0.3\,\%$ (^{3}He) and $< 0.6\,\%$ (^{4}He) for the Labyrinth samples. Standards were reproducible within $< 2\,\%$, and standard sizes ranged from $\sim 4.0 \times 10^{-18}$–1.5×10^{-16} mol and 1.7×10^{-13}–6.5×10^{-12} mol for ^{3}He and ^{4}He, respectively. At LDEO, the mean as well as standard deviation of the ^{3}He concentrations measured in the CRONUS-P reference material at the same time as the Labyrinth core samples was $(5.16 \pm 0.19) \times 10^9$ atoms g^{-1} ($n = 5$, coefficient of variance (CV) = 4 %; Table S3).

At CRPG, 34 measurements were made on 15 CRPG-prepared Labyrinth core samples, and 5 measurements were made on 5 BGC-prepared Labyrinth core samples. Sample extraction was realized by complete fusion at 1500 °C in our custom-made extraction furnace (Blard, 2021; Zimmermann et al., 2018). Typical blanks were $(2.1 \pm 1.4) \times 10^{-20}$ mol of ^{3}He and $(1.9 \pm 0.1) \times 10^{-15}$ mol of ^{4}He. Extracted gas was then purified, cryofocused at 8 K, and released at 75 K in a gigavolt (GV) split flight tube mass spectrometer to measure ^{3}He and ^{4}He abundances. The mass spectrometer sensitivity was established with the helium standard HESJ made by Matsuda et al. (2002). The helium pressure of the HESJ standard bottle has been calibrated against another reference gas, which has itself been cross-checked against independently calibrated air and pure helium standards of two different mass spectrometers at CRPG (Nancy) (Gayer et al., 2004; Blard et al., 2006). At CRPG, the CRONUS-P ^{3}He concentrations, measured between March and April 2019, were $(5.04 \pm 0.12) \times 10^9$ atoms g^{-1} ($n = 8$, CV = 2 %; Table S3).

At BGC, 32 measurements were made on 14 BGC-prepared Labyrinth core samples, and 5 measurements were made on 3 CRPG-prepared Labyrinth core samples for the purpose of interlaboratory comparison. Cosmogenic-^{3}He measurements at BGC employ a laser "microfurnace" extraction system coupled to a MAP-215 mass spectrometer and are described in detail in Balter-Kennedy et al. (2020). Full process blanks measured by heating empty tantalum packets in the same way as the samples were $148\,600 \pm 4200$ atoms of ^{3}He (error-weighted mean of 12 measurements with a reduced chi-squared value of 1.1) and were not distinguishable from the Faraday cup measurement background for ^{4}He. This is an unusually high process blank for ^{3}He measurements and resulted from the reuse of vacuum components that had previously been part of an extraction system used for argon–argon dating. After additional investigation, these components were found to be contaminated with tritium derived from neutron-irradiated samples. The ^{3}He background is therefore the result of ^{3}He production by tritium decay and diffusive release from the metal components. Although this resulted in a comparatively large ^{3}He background, ^{3}He release during sample processing occurred at a constant rate, and the total contribution was strictly proportional to the duration of sample gas residence in certain sections of the extraction line, so variability in the blank could be minimized by automated control of extraction line timing. Therefore, even though the magnitude of the process blank is large compared to typical extraction systems, the uncertainty in the blank correction at BGC is comparable to other labs, and the overall effect on measurement precision is minimal. After completion of this series of measurements, the offending vacuum line components were replaced. At BGC, ^{3}He concentrations measured in CRONUS-P at the same time as the Labyrinth core samples were $(4.78 \pm 0.08) \times 10^9$ atoms g^{-1} ($n = 5$, CV = 2 %; Table S3).

For the surface samples, we used existing ^{3}He measurements made at LDEO, described in Schaefer et al. (2006; Table 2). Although not used in our calculations, earlier ^{3}He measurements were made and published from these samples at ETH Zurich and Potsdam (Niedermann et al., 2007; Schäfer et al., 1999). ^{3}He measurement uncertainties for the surface samples range from 2 %–3 %. The ^{3}He concentration in sample NXP 93*52, measured alongside the other surface samples and the same sample from which the CRONUS-P reference material was derived, is $(5.21 \pm 0.25) \times 10^9$ atoms g^{-1} (Schaefer et al., 2006).

3.2.3 Cosmogenic-^{10}Be analyses

We extracted beryllium from clean pyroxene at LDEO using a procedure modified from the methods for beryllium extraction from quartz (e.g., Bromley et al., 2014; Kohl and Nishiizumi, 1992; Schaefer et al., 2009; https://www.ldeo.columbia.edu/res/pi/tcn/Lamont_Cosmogenic_Nuclide_Lab/Chemistry_files/LDEO_Be_Chemistry_ver.4.pdf, last access: 30 November 2022). The established procedure for extracting beryllium from quartz includes (1) addition of ^{9}Be carrier, (2) sample dissolution, (3) ion exchange chromatography using anion and then cation exchange columns, (4) beryllium precipitation, (5) combustion, and (6) preparation of accelerator mass spectrometer (AMS) targets. Because of the high cation load present in pyroxenes, Eaves et al. (2018) used small sample sizes (~ 2 g) and large resin volumes (20 mL) for cation exchange chromatography. Nevertheless, they concluded that reduction in the cation load prior to ion chromatography using a precipitation step would improve the extraction of beryllium from pyroxene. Here, we add a simple pH 8 precipitation step to reduce the cation load in our samples prior to ion exchange chromatography. At pH 8, Be, Al, and Fe precipitate from solution as hydroxides, $Be(OH)_2$, $Al(OH)_3$, and $Fe(OH)_2$, while Ca and Mg should remain in solution (Ochs and Ivy-Ochs, 1997). We summarize the LDEO methodology for pyroxene here.

For beryllium extraction from pure pyroxene separates we first weighed and spiked 100–200 mg of pyroxene with $\sim$ 180 µg of ^{9}Be using an LDEO carrier (Schaefer et al., 2009). The addition of a ^{9}Be carrier contributed less than 5.7×10^3 atoms of ^{10}Be, which is the average value of our process blanks. The small sample sizes were sufficient for these samples with high cosmogenic-nuclide inventories while mini-

mizing the overall ion load. Samples were digested in concentrated HF and HNO_3 and evaporated to dryness with two to three additions of perchloric acid to drive off fluorides. The resulting residue was taken up in 1 mL 6M HCl, transferred to 15 mL centrifuge tubes, and diluted with 10 mL of Milli-Q water. NH_4OH was used to adjust the pH to 8, discarding the supernatant containing Ca, Mg, and Na and collecting the precipitate containing Be (and Al, Fe, and Ti).

We isolated beryllium using ion chromatography methods described by Kohl and Nishiizumi (1992). Given that most Ca and Mg were likely removed in the pH 8 precipitation step, we opted to use 2 mL of Bio-Rad 50W-X8 200–400 mesh resin for cation exchange based on the amount of Al in our samples (Table S1). Following cation exchange columns, the beryllium fraction was evaporated to dryness and then taken up in 4 mL of 1 % HNO_3, transferred to 15 mL centrifuge tubes. From this solution, we precipitated $Be(OH)_2$ by adjusting the pH to 9 with NH_4OH. After pouring off the supernate, this precipitation step was repeated. We then performed three rinses of the precipitate with Milli-Q water adjusted to pH 8. The $Be(OH)_2$ precipitates were noticeably larger than the blank for several samples (Fig. S3), indicating that we exceeded the capacity of the cation exchange resin and Al or another cation eluted with beryllium. For these samples, we performed a second round of cation exchange chromatography, also with 2 mL of resin. Following the second round of cation columns, the $Be(OH)_2$ precipitates for all samples were similar in size to the blank, indicating that the second column step was successful in isolating beryllium.

The isolated beryllium was then combusted to form BeO, which we combined with Nb powder at an approximate BeO : Nb ratio of 2 : 3 by volume and loaded into stainless-steel AMS cathodes. Packed targets were sent to the Center for Accelerator Mass Spectrometry at Lawrence Livermore National Laboratory for $^{10}Be/^{9}Be$ measurement relative to the 07KNSTD standard with a $^{10}Be/^{9}Be$ ratio of 2.85×10^{-12} (Nishiizumi et al., 2007). Reported uncertainties in ^{10}Be measurements include 1σ uncertainty in the AMS measurement, uncertainty in the blank correction, and error in the carrier concentration (1.5 %) propagated in quadrature.

$^{10}Be/^{9}Be$ ratios in all 15 samples range from 4×10^{-15} to 6×10^{-13}, with relative AMS uncertainties of < 2 %–8 % (Table S4). $^{10}Be/^{9}Be$ ratios for all process blanks are on the order of 10^{-16}, equating to 3000–10 500 atoms of ^{10}Be (Table S5). Therefore, blank corrections for the surface samples are < 0.5 % and between 1 %–7.3 % for the Labyrinth core samples.

3.3 Apparent exposure age and erosion rate calculations

We calculate apparent exposure ages and erosion rates using Version 3 of the online calculator described by Balco et al. (2008) and subsequently updated (http://hess.ess.washington.edu/math/v3/v3_age_in.html, last access: 30 November 2022). All calculations employ the "St" scaling method of Stone (2000) and Lal (1991). To calculate the ^{3}He production rate, we use the primary ^{3}He production rate dataset of Borchers et al. (2016) in Version 3 of the online calculator (120 atoms g^{-1} yr^{-1}; Balco et al., 2008). Apparent exposure ages are calculated assuming zero erosion and equate to a minimum age for the sample. Apparent erosion rates assume infinite exposure time and represent a maximum erosion rate for the sample. Ferrar dolerite pyroxenes are known to contain non-cosmogenic ^{3}He, which is most likely produced by neutron capture on Li via the reaction $^{6}Li(n,\alpha)^{3}He$ (Ackert and Kurz, 2004; Andrews and Kay, 1982). In Ferrar dolerite, the total concentration of non-cosmogenic ^{3}He has been measured in samples that are shielded from the cosmic-ray flux (Ackert, 2000; Kaplan et al., 2017; Margerison et al., 2005). Together, these measurements converge on $(3.3 \pm 1.1) \times 10^{6}$ atoms g^{-1} of non-cosmogenic ^{3}He throughout this lithology (see discussion in Balco, 2020). Non-cosmogenic ^{3}He therefore constitutes < 1 % of the measured ^{3}He in the surface samples, so we do not consider non-cosmogenic ^{3}He significant when calculating apparent exposure ages or erosion rates. At depth in the Labyrinth core, however, non-cosmogenic ^{3}He comprises as much as 10 % of the measured ^{3}He. Therefore, we do include non-cosmogenic ^{3}He when performing production rate calculations in Sect. 5.1.1 and 5.1.2.

4 Results

The new ^{3}He and ^{10}Be data are shown in Tables 1 and 2 and in Figs. 3 and 4. Key features of these datasets are summarized below.

4.1 Cosmogenic-^{3}He concentrations

Cosmogenic-^{3}He concentrations normalized using CRONUS-P in the surface samples range from 0.50–5.87×10^{9} atoms g^{-1}, equating to apparent surface exposure ages of 1.2–6.3 Myr (Table 2). In the Labyrinth dolerite core, CRONUS-P-normalized ^{3}He concentrations range from $(4.75 \pm 0.08) \times 10^{8}$ at the surface to $(0.29 \pm 0.01) \times 10^{8}$ at 164 cm depth (Table 3, Fig. 3). The ^{3}He concentration of the surface sample equates to an apparent exposure age of 1.2 Myr or an apparent erosion rate of 43.8 cm Myr^{-1} (Table 2). Measured cosmogenic-^{3}He concentrations in the Labyrinth core differ slightly among the three labs (Table 3), but normalizing to CRONUS-P brings the BGC-prepared and LDEO-prepared concentrations into agreement within ~ 5 % (Fig. 3). The CRONUS-P-normalized ^{3}He concentrations for the CRPG-prepared samples, however, are systematically lower than the LDEO-prepared and BGC-prepared samples (up to ~ 15 % lower). This is true also for the CRPG-prepared samples that were measured at BGC. Higher-than-expected Al concentrations measured

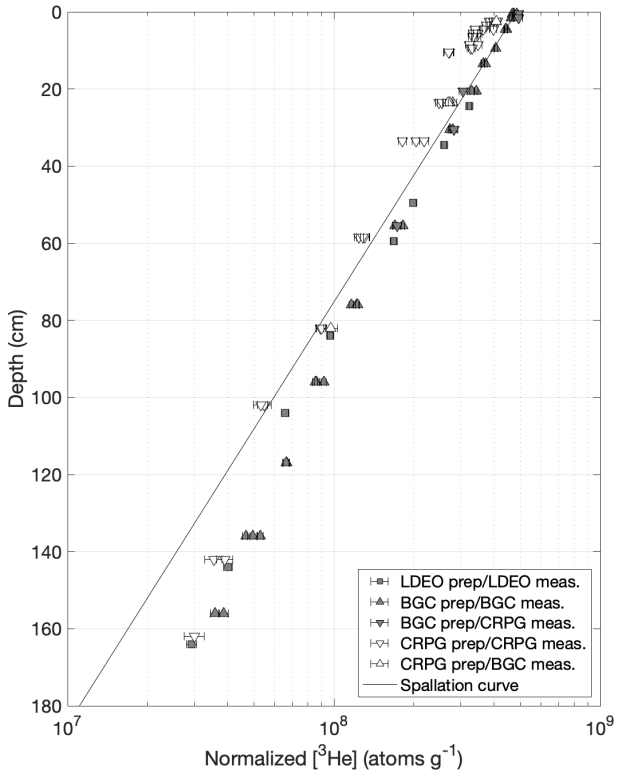

Figure 3. ^{3}He concentrations from the Labyrinth core normalized to CRONUS-P. The CRPG-prepared samples were excluded from the fitting procedure as described in Sect. 5.1.1. The solid black line is an exponential curve showing expected spallation-produced ^{3}He concentrations calculated using the surface ^{3}He concentration and an attenuation length of 140 g cm^{-2}. Below $\sim$ 40 cm depth, the measured ^{3}He concentrations are greater than the spallation curve, presumably due to production by muons.

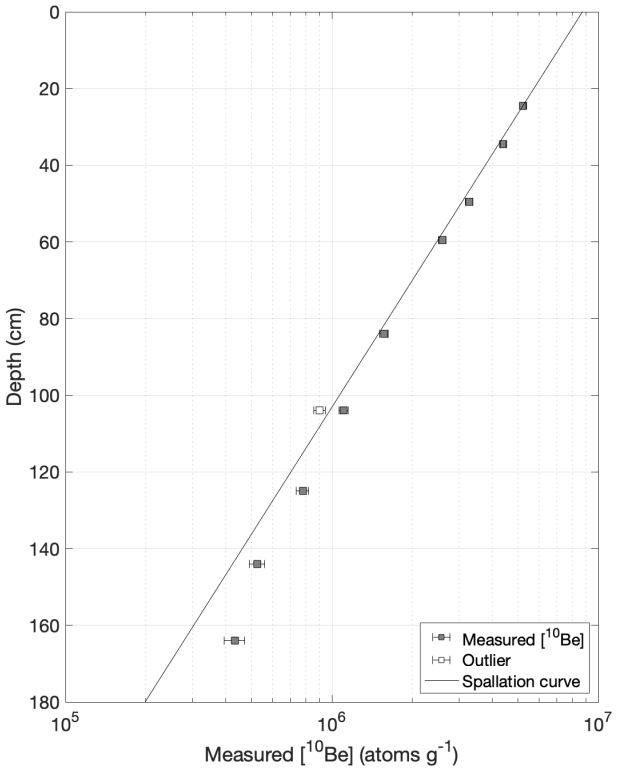

Figure 4. Measured ^{10}Be concentrations in pyroxenes from the Labyrinth core. All samples were prepared at LDEO, and ^{10}Be / ^{9}Be ratios were measured at Lawrence Livermore National Laboratory (LLNL). The black line is an exponential curve showing the expected concentration of spallation-produced ^{10}Be, calculated using the measured ^{10}Be concentration at 24 cm depth and an attenuation length of 140 g cm^{-2}. Below $\sim$ 100 cm depth, the measured ^{10}Be concentrations are greater than the spallation curve, indicating production by muons.

by ICP-OES in the CRPG-prepared pyroxene suggest that plagioclase remained in the CRPG-prepared samples (Tables S1 and S2). To confirm, we applied a mixing model to determine the percentage of pyroxene, plagioclase, and magnetite (a common accessory mineral in Ferrar dolerite) in the CRPG samples and found that the CRPG-prepared samples contain > 10 % plagioclase (see Supplement). The contamination by plagioclase is the likely reason for the lower ^{3}He concentrations in the CRPG-prepared samples because ^{3}He is poorly retained in that mineral phase (Cerling, 1990). Therefore, we exclude the ^{3}He measurements of the CRPG-prepared pyroxenes from further discussion. The observation that plagioclase-contaminated pyroxene samples yielded lower ^{3}He concentrations further supports the use of HF etching as an effective method for producing pure pyroxene separates, as plagioclase is readily dissolved in HF (Bromley et al., 2014). Notably, the ^{4}He concentrations were systematically higher in the non-etched BGC-prepared (and CRPG-prepared) samples than in the LDEO-prepared samples, which were HF-etched (Fig. S2).

4.2 Cosmogenic-^{10}Be concentrations

^{10}Be concentrations in the six surface samples range from 1.02–5.06 $\times$ 10^{7} atoms g^{-1}, with corresponding uncertainties of $\sim$ 2 %. Nine ^{10}Be concentrations between 24 and 164 cm depth in the Labyrinth bedrock core ranged from 5.21 $\times$ 10^{6} atoms g^{-1} in the uppermost sample to 4.32 $\times$ 10^{5} atoms g^{-1} in the lowermost sample (Table 3, Fig. 4). Our first ^{10}Be measurement of the Labyrinth core sample LABCO-06 clearly deviates from the rest of the depth profile, although the reasons for this are unknown. A second measurement of a re-processed split of LABCO-06, however, agrees with the rest of the ^{10}Be concentrations in the depth profile. Therefore, in the production rate calibration exercise described in Sect. 5.1.1, we use only the second measurement of LABCO-06. Total relative uncertainty (measurement error, blank correction, and error in the carrier concentration propagated in quadrature) increased from 3 %–9 % downcore.

Table 3. Cosmogenic-nuclide concentrations for the Labyrinth core.

Sample ID	Average depth (cm)	Aliquot	Sample weight for ^{3}He analysis (g)	Measured [^{3}He] (atoms g^{-1})	[^{3}He] normalized to CRONUS-P (atoms g^{-1})	[^{3}He] error (atoms g^{-1})	[^{4}He] (atoms g^{-1})	[^{4}He] error (atoms g^{-1})	Measured [^{10}Be] (atoms g^{-1})	[^{10}Be] error (atoms g^{-1})	Lab for pyroxene separation	Lab for ^{3}He analysis
LABCO-01	24.5	a		3.31E+08	3.22E+08	6.18E+06	5.90E+13	8.44E+11	5.21E+06	1.45E+05	LDEO	LDEO
LABCO-02	34.5	a		2.66E+08	2.59E+08	5.24E+06	6.58E+13	9.36E+11	4.39E+06	1.17E+05	LDEO	LDEO
LABCO-03	49.5	a		2.04E+08	1.98E+08	5.26E+06	7.45E+13	2.41E+12	3.28E+06	1.06E+05	LDEO	LDEO
LABCO-04	59.5	a		1.73E+08	1.68E+08	4.37E+06	5.93E+13	2.08E+12	2.60E+06	8.11E+04	LDEO	LDEO
LABCO-05	84	a		9.96E+07	9.69E+07	2.34E+06	5.56E+13	7.95E+11	1.57E+06	5.90E+04	LDEO	LDEO
LABCO-06 (no. 1)	104	a		6.74E+07	6.56E+07	2.07E+06	3.85E+13	2.04E+12	9.01E+05	4.59E+04	LDEO	LDEO
LABCO-06 (no. 2)	104	a	–	–	–	–	–	–	1.11E+06	4.32E+04	LDEO	LDEO
LABCO-07	125	a	–	–	–	–	–	–	7.78E+05	4.22E+04	LDEO	LDEO
LABCO-08	144	a		4.11E+07	4.00E+07	1.47E+06	4.81E+13	2.11E+12	5.25E+05	3.54E+04	LDEO	LDEO
LABCO-09	164	a		3.00E+07	2.92E+07	1.24E+06	4.12E+13	2.01E+12	4.32E+05	3.86E+04	LDEO	LDEO
DOL_3	2.5	a	0.0108	3.85E+08	3.83E+08	1.02E+07	1.47E+14	1.11E+12	–	–	CRPG	CRPG
DOL_3_bis	2.5	b	0.0103	4.14E+08	4.12E+08	1.11E+07	1.28E+14	9.85E+11	–	–	CRPG	CRPG
DOL_3_a	2.5	c	0.0045	3.99E+08	3.97E+08	1.36E+07	2.27E+14	1.81E+12	–	–	CRPG	CRPG
DOL_3_a	2.5	a	0.0117	3.88E+08	4.07E+08	1.56E+07	1.83E+14	6.42E+12	–	–	CRPG	BGC
DOL_4	3.5	a	0.0106	3.89E+08	3.87E+08	1.01E+07	1.88E+14	1.39E+12	–	–	CRPG	CRPG
DOL_4_b	3.5	b	0.0051	3.76E+08	3.74E+08	1.38E+07	2.08E+14	1.65E+12	–	–	CRPG	CRPG
DOL_5	4.5	a	0.0103	3.65E+08	3.64E+08	9.32E+06	3.07E+14	1.18E+12	–	–	CRPG	CRPG
DOL_5_a	4.5	b	0.0051	3.41E+08	3.39E+08	1.23E+07	2.72E+14	2.10E+12	–	–	CRPG	CRPG
DOL_5_b	4.5	c	0.0052	3.99E+08	3.97E+08	1.27E+07	1.34E+14	1.16E+12	–	–	CRPG	CRPG
DOL_6_a	5.5	a	0.0049	3.35E+08	3.33E+08	1.17E+07	1.50E+14	1.28E+12	–	–	CRPG	CRPG
DOL_6_b	5.5	b	0.0047	3.48E+08	3.47E+08	1.22E+07	2.14E+14	1.78E+12	–	–	CRPG	CRPG
DOL_7	6.5	a	0.0107	3.40E+08	3.38E+08	9.19E+06	1.30E+14	9.94E+11	–	–	CRPG	CRPG
DOL_7_a	6.5	b	0.0048	3.45E+08	3.43E+08	1.25E+07	1.57E+14	1.33E+12	–	–	CRPG	CRPG
DOL_7_b	6.5	c	0.0048	3.33E+08	3.32E+08	1.26E+07	1.36E+14	1.20E+12	–	–	CRPG	CRPG
DOL_9_a	8.5	a	0.0048	3.49E+08	3.48E+08	1.16E+07	2.33E+14	1.83E+12	–	–	CRPG	CRPG
DOL_9_b	8.5	b	0.0049	3.25E+08	3.23E+08	1.16E+07	1.97E+14	1.59E+12	–	–	CRPG	CRPG
DOL_10	9.5	a	0.0101	3.27E+08	3.26E+08	9.45E+06	1.55E+14	1.17E+12	–	–	CRPG	CRPG
DOL_10_bis	9.5	b	0.0107	3.32E+08	3.30E+08	9.18E+06	1.22E+14	9.38E+11	–	–	CRPG	CRPG
DOL_11_a	10.5	a	0.0047	2.72E+08	2.71E+08	1.12E+07	1.75E+14	1.45E+12	–	–	CRPG	CRPG
DOL_11_b	10.5	b	0.0052	2.71E+08	2.69E+08	1.08E+07	1.55E+14	1.30E+12	–	–	CRPG	CRPG
DOL_13	23.5	a	0.0109	2.50E+08	2.49E+08	7.38E+06	1.77E+14	1.31E+12	–	–	CRPG	CRPG
DOL_13_b	23.5	b	0.005	2.56E+08	2.54E+08	9.83E+06	1.69E+14	1.40E+12	–	–	CRPG	CRPG
CRPG-DOL13a	23.5	a	0.01764	2.65E+08	2.79E+08	1.08E+07	1.83E+14	6.40E+12	–	–	CRPG	BGC
CRPG-DOL13b	23.5	b	0.0185	2.59E+08	2.72E+08	1.03E+07	1.74E+14	6.05E+12	–	–	CRPG	BGC
CRPG-DOL13c	23.5	c	0.01614	2.55E+08	2.68E+08	1.06E+07	2.06E+14	7.22E+12	–	–	CRPG	BGC
DOL_14	33.5	a	0.0102	1.82E+08	1.81E+08	6.12E+06	2.09E+14	1.53E+12	–	–	CRPG	CRPG
DOL_14_bis	33.5	b	0.0102	2.05E+08	2.04E+08	6.53E+06	1.58E+14	1.19E+12	–	–	CRPG	CRPG
DOL_14_b	33.5	c	0.0051	2.20E+08	2.19E+08	8.87E+06	2.13E+14	1.68E+12	–	–	CRPG	CRPG
DOL_16	58.5	a	0.0106	1.31E+08	1.31E+08	4.83E+06	1.48E+14	1.11E+12	–	–	CRPG	CRPG
DOL_16_bis	58.5	b	0.0101	1.25E+08	1.24E+08	4.92E+06	1.83E+14	1.36E+12	–	–	CRPG	CRPG
DOL_16_c	58.5	c	0.0048	1.29E+08	1.29E+08	7.33E+06	1.84E+14	1.51E+12	–	–	CRPG	CRPG
DOL_17	82	a	0.0107	8.96E+07	8.92E+07	3.85E+06	1.94E+14	1.43E+12	–	–	CRPG	CRPG
DOL_17_bis	82	b	0.0104	9.03E+07	8.99E+07	3.95E+06	1.68E+14	1.25E+12	–	–	CRPG	CRPG

Table 3. Continued.

Sample ID	Average depth (cm)	Aliquot	Sample weight for ^{3}He analysis (g)	Measured (^{3}He) (atoms g^{-1})	(^{3}He) normalized to CRONUS-P (atoms g^{-1})	(^{3}He) error (atoms g^{-1})	(^{4}He) (atoms g^{-1})	(^{4}He) error (atoms g^{-1})	Measured (^{10}Be) (atoms g^{-1})	(^{10}Be) error (atoms g^{-1})	Lab for pyroxene separation	Lab for ^{3}He analysis
CRPG-DOL17a	82	a	0.01593	9.28E+07	9.75E+07	5.79E+06	1.96E+14	6.90E+12	–	–	CRPG	BGC
DOL_18	102	a	0.0105	5.51E+07	5.49E+07	3.20E+06	1.80E+14	1.33E+12	–	–	CRPG	CRPG
DOL_18_bis	102	b	0.0102	5.34E+07	5.32E+07	3.27E+06	2.13E+14	1.56E+12	–	–	CRPG	CRPG
DOL_20	142	a	0.01	3.92E+07	3.90E+07	2.69E+06	1.48E+14	1.12E+12	–	–	CRPG	CRPG
DOL_20_bis	142	b	0.0105	3.55E+07	3.54E+07	2.65E+06	1.27E+14	9.78E+11	–	–	CRPG	CRPG
DOL_21	162	a	0.0104	3.01E+07	3.00E+07	2.57E+06	2.45E+14	9.88E+11	–	–	CRPG	CRPG
LABCO-0-1-Px	0.5	b	0.0403	4.52E+08	4.75E+08	7.81E+06	1.55E+14	1.35E+12	–	–	BGC	BGC
LABCO-0-1-Px	0.5	c	0.02991	4.45E+08	4.67E+08	5.08E+06	1.60E+14	4.64E+11	–	–	BGC	BGC
LABCO-0-1-Px	0.5	d	0.02234	4.64E+08	4.87E+08	6.08E+06	1.99E+14	5.78E+11	–	–	BGC	BGC
LABCO-0-1-Px	0.5	a	0.0325	4.95E+08	4.93E+08	1.63E+07	1.48E+14	5.45E+11	–	–	BGC	CRPG
LABCO-1-2-Px	1.5	b	0.0492	4.41E+08	4.63E+08	7.45E+06	2.00E+14	1.52E+12	–	–	BGC	BGC
LABCO-1-2-Px	1.5	c	0.0259	4.45E+08	4.68E+08	5.30E+06	2.22E+14	6.53E+11	–	–	BGC	BGC
LABCO-1-2-Px	1.5	a	0.0305	4.97E+08	4.95E+08	1.75E+07	2.36E+14	9.20E+12	–	–	BGC	CRPG
LABCO-4-5-Px	4.5	a	0.0336	4.20E+08	4.41E+08	7.31E+06	2.06E+14	1.59E+12	–	–	BGC	BGC
LABCO-4-5-Px	4.5	b	0.02657	4.23E+08	4.44E+08	5.49E+06	2.31E+14	9.02E+11	–	–	BGC	BGC
LABCO-4-5-Px	4.5	c	0.02037	4.20E+08	4.41E+08	5.72E+06	2.10E+14	6.16E+11	–	–	BGC	BGC
LABCO-9-10-Px	9.5	b	0.0287	3.86E+08	4.05E+08	6.83E+06	1.96E+14	1.49E+12	–	–	BGC	BGC
LABCO-9-10-Px	9.5	c	0.01913	3.86E+08	4.06E+08	5.19E+06	1.89E+14	5.54E+11	–	–	BGC	BGC
LABCO-13-14-Px	13.5	a	0.0324	3.46E+08	3.63E+08	6.27E+06	2.01E+14	1.54E+12	–	–	BGC	BGC
LABCO-13-14-Px	13.5	b	0.01797	3.46E+08	3.64E+08	5.19E+06	1.85E+14	5.39E+11	–	–	BGC	BGC
LABCO-13-14-Px	13.5	c	0.01696	3.54E+08	3.71E+08	4.92E+06	2.07E+14	6.03E+11	–	–	BGC	BGC
LABCO-20-21-Px	20.5	b	0.0238	3.26E+08	3.43E+08	5.66E+06	1.89E+14	1.25E+12	–	–	BGC	BGC
LABCO-20-21-Px	20.5	c	0.0365	3.14E+08	3.29E+08	5.65E+06	2.03E+14	1.67E+12	–	–	BGC	BGC
LABCO-20-21-Px	20.5	a	0.0982	3.07E+08	3.06E+08	1.04E+07	1.97E+14	7.69E+12	–	–	BGC	CRPG
LABCO-30-31-Px	30.5	b	0.0434	2.60E+08	2.73E+08	4.10E+06	2.25E+14	1.50E+12	–	–	BGC	BGC
LABCO-30-31-Px	30.5	c	0.0355	2.65E+08	2.79E+08	4.84E+06	2.33E+14	1.80E+12	–	–	BGC	BGC
LABCO 30-31	30.5	a	0.0524	2.84E+08	2.82E+08	1.00E+07	2.01E+14	7.84E+12	–	–	BGC	CRPG
LABCO-55-56-Px	55.5	b	0.0388	1.62E+08	1.70E+08	3.13E+06	1.74E+14	1.33E+12	–	–	BGC	BGC
LABCO-55-56-Px	55.5	c	0.03096	1.73E+08	1.81E+08	2.87E+06	1.77E+14	5.19E+11	–	–	BGC	BGC
LABCO 55-56	55.5	a	0.0367	1.73E+08	1.73E+08	6.64E+06	1.74E+14	6.77E+12	–	–	BGC	CRPG
LABCO-75-77-Px	76	c	0.0467	1.11E+08	1.16E+08	2.33E+06	2.34E+14	1.80E+12	–	–	BGC	BGC
LABCO-75-77-Px	76	d	0.01901	1.16E+08	1.21E+08	2.61E+06	2.38E+14	7.03E+11	–	–	BGC	BGC
LABCO-75-77-Px	76	e	0.02863	1.17E+08	1.23E+08	2.18E+06	2.11E+14	6.09E+11	–	–	BGC	BGC
LABCO-95-97-Px	96	a	0.0433	8.72E+07	9.16E+07	2.09E+06	2.25E+14	1.74E+12	–	–	BGC	BGC
LABCO-95-97-Px	96	c	0.02561	8.20E+07	8.61E+07	1.96E+06	2.22E+14	6.50E+11	–	–	BGC	BGC
LABCO-95-97-Px	96	d	0.02879	8.09E+07	8.50E+07	1.95E+06	2.37E+14	6.92E+11	–	–	BGC	BGC
LABCO-116-118-Px	117	c	0.03119	6.32E+07	6.63E+07	1.71E+06	2.64E+14	7.75E+11	–	–	BGC	BGC
LABCO-116-118-Px	117	d	0.02954	6.28E+07	6.60E+07	1.76E+06	2.47E+14	7.18E+11	–	–	BGC	BGC
LABCO-135-137-Px	136	b	0.03351	4.46E+07	4.68E+07	1.53E+06	2.02E+14	5.86E+11	–	–	BGC	BGC
LABCO-135-137-Px	136	c	0.02165	4.72E+07	4.95E+07	2.03E+06	2.04E+14	5.97E+11	–	–	BGC	BGC
LABCO-135-137-Px	136	d	0.04114	5.03E+07	5.28E+07	1.39E+06	2.04E+14	5.96E+11	–	–	BGC	BGC
LABCO-155-157-Px	156	c	0.02429	3.66E+07	3.85E+07	1.60E+06	1.39E+14	4.28E+11	–	–	BGC	BGC
LABCO-155-157-Px	156	d	0.03131	3.40E+07	3.57E+07	1.41E+06	1.48E+14	4.26E+11	–	–	BGC	BGC

Geochronology, 5, 301–321, 2023 https://doi.org/10.5194/gchron-5-301-2023

Using a previously published production rate for ^{10}Be in pyroxene of 3.6 atoms g^{-1} yr^{-1} (Eaves et al., 2018), the apparent ^{10}Be exposure ages of the surface samples range from 1.0–4.4 Myr, and the apparent ^{10}Be exposure age of the Labyrinth core surface is $\sim$ 830 kyr (surface ^{10}Be concentration calculated by fitting an exponential curve to the ^{10}Be data; therefore, surface ^{10}Be age for the Labyrinth core is approximate).

4.3 General observations

Here, we highlight several key features of our dataset that inform the production rate estimations in Sect. 5.1. First, we observe that the apparent ^{3}He and ^{10}Be ages are discordant in surface samples 318, 444, 464, and 446S and the Labyrinth core surface (Table 2), suggesting that these samples have experienced complex exposure histories, potentially involving subaerial erosion or burial (e.g., by ice or sediment) or both. The canonical interpretation is that the geomorphic setting of these sample locations is consistent with a single period of exposure (Sect. 2), so a likely reason for this discordance is subaerial erosion. This observation requires that we consider erosion when attempting to estimate spallation and muon production rates in Sect. 5.1.

Figures 3 and 4 show that the measured ^{10}Be and ^{3}He inventories in the Labyrinth core exceed those predicted by a spallation curve below $\sim$ 100 cm depth and $\sim$ 40 cm depth, respectively, indicating that muon-produced ^{10}Be and ^{3}He make up a significant portion of the measured concentrations below these depths. With this finding, we present the first identification of in situ ^{10}Be production by muons and further confirm the importance of quantifying muon production of ^{3}He (Larsen et al., 2021). At the depth range of the Labyrinth core, negative-muon capture is the primary muon production pathway. Therefore, we can use these data to estimate the negative-muon cross-sections for ^{3}He and ^{10}Be in pyroxene (Sect. 5.1.1).

5 Discussion

5.1 Production rate estimate

The goal of this section is to place limits on several key parameters associated with ^{10}Be and ^{3}He production in pyroxene. Here, we use our Labyrinth core data to estimate parameters associated with spallation production of ^{10}Be and ^{10}Be and ^{3}He production by negative-muon capture. In addition to the Labyrinth core, we use the surface sample data to further refine the ^{10}Be spallation production rate in pyroxene. After estimating a production rate for each sample, we combine our findings from the Labyrinth core and surface samples to arrive at a likely value for the ^{10}Be spallation production rate.

5.1.1 Spallation and muon production in the Labyrinth core

We use the ^{10}Be and ^{3}He concentrations in pyroxenes from the Labyrinth core to estimate parameters associated with ^{10}Be and ^{3}He production. To do so, we apply a forward model, adapted from Balco et al. (2019) to include radioactive decay, that simulates the accumulation of cosmogenic ^{3}He and ^{10}Be by spallation and muon production with depth. We then estimate several parameters related to ^{10}Be and ^{3}He production in pyroxene by fitting the model to our measured ^{10}Be and ^{3}He concentrations.

Measured ^{3}He includes cosmogenic ^{3}He produced by neutron spallation, negative-muon capture, fast-muon interactions, and non-cosmogenic ^{3}He:

$$\mathrm{N_{3,\,m}} = \mathrm{N_{3,\,sp}} + \mathrm{N_{3,\,\mu^-}} + \mathrm{N_{3,\,\mu f}} + \mathrm{N_{3,\,non\text{-}cosmo}}\,. \quad (1)$$

$\mathrm{N_{3,\,m}}$ (atoms g^{-1}) is the measured ^{3}He concentration, $\mathrm{N_{3,\,sp}}$ (atoms g^{-1}) is ^{3}He produced by high-energy neutron spallation, $\mathrm{N_{3,\,\mu^-}}$ (atoms g^{-1}) is ^{3}He produced by negative-muon capture, and $\mathrm{N_{3,\,\mu f}}$ (atoms g^{-1}) is ^{3}He produced by fast-muon reactions. $\mathrm{N_{3,\,non\text{-}cosmo}}$ (atoms g^{-1}) is non-cosmogenic ^{3}He, which we consider to be $(3.3 \pm 1.1) \times 10^{6}$ atoms g^{-1} in Ferrar pyroxenes (see Sect. 3.3 and discussion in Balco, 2020).

In contrast, all the measured ^{10}Be is cosmogenic, produced by spallation and muon interactions:

$$\mathrm{N_{10,\,m}} = \mathrm{N_{10,\,sp}} + \mathrm{N_{10,\,\mu^-}} + \mathrm{N_{10,\,\mu f}}\,. \quad (2)$$

Cosmogenic-nuclide production by high-energy neutron spallation decreases exponentially with mass depth (Lal, 1991):

$$\mathrm{P}_{i,\,\mathrm{sp}}(z) = \mathrm{P}_{i,\,\mathrm{sp}}(0) e^{-\frac{z}{\Lambda_{\mathrm{sp}}}}\,, \quad (3)$$

where z is mass depth below the surface (g cm^{-2}), $\mathrm{P}_{i,\,\mathrm{sp}}(0)$ is the surface production rate of a given nuclide (atoms g^{-1} yr^{-1}), and Λ_{sp} is the effective attenuation length for spallation production in mass depth (g cm^{-2}). Therefore, the concentration of spallation-produced ^{3}He as a function of mass depth z is

$$\begin{aligned}\mathrm{N_{3,\,sp}}(z) &= \mathrm{P_{3,\,sp,\,SLHL}} \times S_{\mathrm{St}} \int_0^t e^{-\frac{z+\varepsilon\tau}{\Lambda_{\mathrm{sp}}}}\,\mathrm{d}\tau \\ &= \frac{\mathrm{P_{3,\,sp,\,SLHL}} \times S_{\mathrm{St}} \times e^{-\frac{z}{\Lambda_{\mathrm{sp}}}} \Lambda_{\mathrm{sp}}}{\varepsilon}\left(1 - e^{-\frac{\varepsilon t}{\Lambda_{\mathrm{sp}}}}\right), \quad (4)\end{aligned}$$

where $\mathrm{P_{3,\,sp,SLHL}}$ is the reference production rate for ^{3}He at sea-level high latitude (SLHL), S_{St} is the scaling factor using St scaling (Stone, 2000), t is the exposure duration (yr), ε is the surface erosion rate (g cm^{-2} yr^{-1}), and τ is a variable of integration. The concentration of spallation-produced ^{10}Be,

a radionuclide, as a function of mass depth z is

$$N_{10,\,sp}(z) = P_{10,\,sp,SLHL} \times S_{St} \int_0^t e^{-(\lambda_{10}+\frac{z+\varepsilon\tau}{\Lambda sp})\tau} d\tau$$

$$= \frac{P_{10,\,sp,SLHL} \times S_{St} \times e^{-\frac{z}{\Lambda sp}}}{\lambda_{10} + \frac{\varepsilon}{\Lambda sp}} (1 - e^{-(\lambda_{10}+\frac{\varepsilon}{\Lambda sp})t}), \quad (5)$$

where $P_{10,\,sp,SLHL}$ is the SLHL reference production rate for ^{10}Be, and λ_{10} is the decay constant for ^{10}Be (5.00×10^{-7} yr^{-1}; Chmeleff et al., 2010; Fink and Smith, 2007; Korschinek et al., 2010).

We adopt production by negative-muon capture from Heisinger et al. (2002b) as

$$N_{3,\,\mu^-} = f_3^* f_C f_D \int_0^t R_{\mu^-}(z + \varepsilon\tau) d\tau \quad (6)$$

$$N_{10,\,\mu^-} = f_{10}^* f_C f_D \int_0^t R_{\mu^-}(z + \varepsilon\tau) e^{-\lambda\tau} d\tau\,, \quad (7)$$

where R_{μ^-} is the muon stopping rate, f_D is the probability that the negative muon does not decay in the K shell before capture by the nucleus, f_C is the chemical compound factor, and f_i^* is the probability that the nuclide of interest is produced after negative-muon capture by the target nucleus. For muon-produced ^{10}Be, the target nucleus is O, and we aim to find the optimal value for f_{10}^*, which should be the same as the value of this parameter calibrated in quartz (0.00191; Balco, 2017). For O in a Ferrar dolerite pyroxene with composition $En_{34}Fs_{25}Wo_{42}$ (typical augite from a medium-grained dolerite; Zavala et al., 2011), $f_C = 0.520$ (von Egidy and Hartmann, 1982); f_D is well known for O (0.1828; Suzuki et al., 1987). In contrast, ^{3}He is produced in many negative-muon-capture reactions on a myriad of targets (see Table 3 in Heisinger et al., 2002b). Therefore, we estimate the entire $f_3^* f_C f_D$ term, which represents the overall probability that a negative muon produces ^{3}He. The $f_3^* f_C f_D$ term should be similar to 0.0045, which is the sum of theoretical $f_3^* f_C f_D$ values for ^{3}He and ^{3}H producing reactions in standard rock (Nesterenok and Yakubovich, 2016).

Production by fast-muon interactions is taken from Heisinger et al. (2002a) as

$$N_{3,\,\mu f} = \sigma_{0,3} N_{pyx} \int_0^t \beta(z + \varepsilon\tau)\phi(z + \varepsilon\tau)\overline{E}^{\alpha}(z + \varepsilon\tau) d\tau \quad (8)$$

$$N_{10,\,\mu f} = \sigma_{0,10} N_{O,\,pyx} \int_0^t \beta(z + \varepsilon\tau)\phi(z + \varepsilon\tau)\overline{E}^{\alpha}(z + \varepsilon\tau) e^{-\lambda\tau} d\tau\,. \quad (9)$$

Here, $\sigma_{0,i}$ is the cross-section for nuclide production by fast muons. Because the Labyrinth core does not extend to depths dominated by fast-muon production, meaning that we cannot estimate the fast-muon cross-sections with our dataset, we apply fast-muon cross-sections from other studies in our model. We take $\sigma_{0,10}$ to be the same as quartz (0.280 µb; Balco, 2017) and $\sigma_{0,3}$ to be 6.01 µb, calculated by fitting Eq. 8 to ^{3}He measurements in pyroxene from a 300 m drill core of the Columbia River Basalt in Washington, USA (Larsen et al., 2021; see Supplement). N_{pyx} is the number of target atoms per gram in standard basalt, assuming all elements are targets (2.74×10^{22} atoms g^{-1}, average atomic mass 22), and $N_{O,\,pyx}$ is the number of atoms per gram of O (1.57×10^{22} atoms g^{-1}, relevant for ^{10}Be production) for a Ferrar dolerite pyroxene with composition $En_{34}Fs_{25}Wo_{42}$ (Zavala et al., 2011). The remaining terms in these equations yield the integrated muon flux at a given mass depth over time for a prescribed surface erosion rate (see Heisinger et al., 2002a, for symbol definitions). We evaluate Eqs. (8) and (9) using the "Model 1A" MATLAB code of Balco (2017), with the parameter α set to 1 (see discussion in Borchers et al., 2016, and Balco, 2017).

Together, Eqs. (1)–(9) comprise a forward model that we use to predict ^{3}He and ^{10}Be concentrations in our core samples. We apply the known ^{3}He production rate calculated using the primary production dataset of Borchers et al. (2016; see Sect. 3.3), so our model has seven unknown parameters: the exposure duration, t; the surface erosion rate, ε; the spallogenic ^{10}Be production rate at sea-level high latitude (SLHL), $P_{10,\,sp,\,SLHL}$; the spallation attenuation length, Λsp; the probability that negative-muon capture creates ^{3}He and ^{10}Be, $f_3^* f_C f_D$ and f_{10}^* (since f_C and f_D are known for ^{10}Be for the target O), respectively; and a variable to account for the core measurement offset below 18 cm depth (see discussion in Sect. 3.1 regarding discrepancy between the drillers' measurements of the core barrel and the recovered core length). We fit our model by minimizing the χ^2 misfit statistic, M:

$$M = \sum_j \left[\frac{N_{10,\,p,\,j} - N_{10,\,m,\,j}}{\sigma_{10,\,m,\,j}} \right]^2 + \sum_n \left[\frac{N_{3,\,p,\,n} - N_{3,\,m,\,n}}{\sqrt{\sigma_{3,m,n}^2 + \sigma_{3,\,non\text{-}cosmo}^2}} \right]^2, \quad (10)$$

where $N_{i,\,p}$ is the predicted cosmogenic-nuclide concentration, $N_{i,\,m}$ is the measured cosmogenic-nuclide concentration, $\sigma_{i,\,m}$ is the associated measurement uncertainty, and $\sigma_{3,\,non\text{-}cosmo}$ is the uncertainty in the non-cosmogenic-^{3}He concentration in Ferrar dolerite. We impose the constraint that all parameters in this fitting exercise must be greater than zero, except the variable accounting for the core measurement offset below 18 cm, which can have any value.

The exposure history of a sample is important for determining parameters associated with cosmogenic-nuclide production, as burial and erosion affect the accumulation of

cosmogenic nuclides throughout the rock column. Previous work suggests that the Labyrinth has been largely undisturbed since the mid-Miocene (Lewis et al., 2006; Sect. 2). We thus assume that the Labyrinth core site has not experienced burial since the mid-Miocene. Erosion, however, must be considered. Erosion brings rock from lower in the rock column towards the surface. In eroding rock, therefore, the measured nuclide concentration at any given depth accumulated at a range of depths with varying contributions from each of the muon production pathways. Therefore, the muon cross-sections and erosion rates cannot be determined simultaneously since infinite combinations of the two could yield the measured nuclide concentrations.

Because we cannot estimate all unknown parameters at the same time, we consider two end-members that capture the possible ranges for the production rate parameters given our measured ^{10}Be and ^{3}He concentrations. In the first end-member scenario, we assume that the site has experienced a finite period of exposure, determined by the apparent ^{3}He exposure age, and zero erosion. For the second end-member, we assume that the site has been exposed for a much longer time than the apparent exposure age (several ^{10}Be half-lives) at a steady erosion rate. Based on those end-members we can place limits on the parameters associated with ^{10}Be and ^{3}He in pyroxene.

The steady-erosion end-member affords a maximum value for spallation production of ^{10}Be. Solving Eq. (5) for $P_{10,\,sp,\,SLHL}$ at the Earth's surface yields

$$P_{10,\,sp,\,SLHL} = \frac{N_{10}(\lambda_{10} + \frac{\varepsilon}{\Lambda sp})}{S_{St}(1 - e^{-(\lambda_{10} + \frac{\varepsilon}{\Lambda sp})t})}. \quad (11)$$

As $t \to \infty$, $P_{10,\,sp,\,SLHL} = N_{10}(\lambda_{10} + \frac{\varepsilon}{\Lambda sp})/S_{St}$. Because ε must be between zero and ε_3 (the steady erosion rate from the ^{3}He data; Sect. 4.1), $P_{10,\,sp,\,SLHL}$ must be between $(N_{10} \times \lambda_{10})/S_{St}$ and $N_{10}(\lambda_{10} + \frac{\varepsilon_3}{\Lambda sp})/S_{St}$.

The opposite is true for parameters associated with negative-muon capture, where the steady-erosion end-member yields a minimum value for $f_3^* f_C f_D$ and f_{10}^*, and the zero-erosion end-member yields a maximum. Erosion exposes rock that contains cosmogenic nuclides produced at depths where fast muons comprise the majority of production, meaning that, compared to the zero-erosion assumption, the steady-erosion assumption will yield cosmogenic-nuclide concentrations with a higher proportion produced by fast muons and a smaller proportion produced by negative-muon capture. Because we prescribe values for the fast-muon cross-sections, the negative-muon cross-section decreases in our steady-erosion model to accommodate the fast-muon-produced inventory that accumulated when the sample was deeper in the rock column. Therefore, the steady-erosion end-member yields minimum values for $f_3^* f_C f_D$ and f_{10}^*, and the zero-erosion end-member will give maximum values for $f_3^* f_C f_D$ and f_{10}^*. In sum, the zero-erosion end-member will produce a lower limit on the spallation production rate and an upper limit on parameters associated with nuclide production by negative-muon capture, and the steady-erosion end-member affords an upper limit on the spallation production rate and a lower limit on the negative-muon-capture parameters. The optimal values for the production parameters for each end-member are listed in Table 4.

Zero-erosion end-member

In the $\varepsilon = 0\,\mathrm{cm\,yr^{-1}}$ end-member, there remain six unknown parameters: t, $P_{10,sp,SLHL}$, Λsp, $f_3^* f_C f_D$, and f_{10}^* and a variable to account for the core measurement offset below 18 cm. The minimum value of the χ^2 statistic, M, is 111 for 24 degrees of freedom (30 samples minus 6 fitting parameters), resulting in a reduced χ^2 value of 4.6. Because the residuals do not appear systematic (Fig. 5), the likely reason for this high χ^2 value is errors unaccounted for in the misfit statistic, such as the uncertainty associated with interlaboratory standardization.

The results of this fitting exercise are shown in Fig. 5. The best-fitting parameter value for the zero-erosion case is $t = 1.18$ Myr, which agrees with the apparent ^{3}He age at the surface (1.24 Ma; Sect. 4.1). Optimal values for spallation-related parameters in this model are $P_{10,sp,SLHL} = 2.82\,\mathrm{atoms\,g^{-1}\,yr^{-1}}$ and $\Lambda sp = 142\,\mathrm{g\,cm^{-2}}$. As discussed above, $P_{10,sp,SLHL}$ should be a minimum in this end-member, and the optimal value of 2.82 is indeed at the low end of the $P_{10,sp,SLHL}$ confidence interval found in Eaves et al. (2018; reference production rate of $3.6 \pm 0.8\,\mathrm{atoms\,g^{-1}\,yr^{-1}}$ at sea-level high latitude). The fitted value for Λsp is close to other estimates of the spallation attenuation length in Antarctica ($\sim 140\,\mathrm{g\,cm^{-2}}$; Borchers et al., 2016; Balco et al., 2019; Brown et al., 1992), although the attenuation length is expected to vary slightly for different nuclides and lithologies (Argento et al., 2015). The best-fitting value for the measurement offset below 18 cm is 2.12 cm.

The optimal values for parameters related to negative-muon capture in this scenario are $f_{10}^* = 0.00534$ and $f_3^* f_C f_D = 0.05783$. Again, the zero-erosion end-member should yield maximum constraints for these parameters. The optimal value for f_{10}^* is the same magnitude as f_{10}^* for quartz (0.00191; Balco, 2017), while the value for $f_3^* f_C f_D$ is an order of magnitude higher than the expected value of 0.0045 for standard rock (Nesterenok and Yakubovich, 2016).

Steady-erosion end-member

For the steady-erosion end-member, we impose an exposure duration of 14.5 Myr based on ^{39}Ar / ^{40}Ar ages of in situ ash deposits that suggest the Labyrinth formed by $\sim$ 14–15 Ma (Lewis et al., 2006; Sect. 2). With that assumption, the remaining free parameters are ε, $P_{10,sp,SLHL}$, Λsp, $f_3^* f_C f_D$, and f_{10}^* and the depth measurement offset below 18 cm. The same fit is achieved as the zero-erosion case, with a min-

Table 4. Optimal production parameter values for ^{10}Be and ^{3}He in pyroxene in the Labyrinth core.

	Exposure age (Myr)	Erosion rate (cm Myr^{-1})	Λ_{sp} (g cm^{-2})	$P_{10,sp,SLHL}$ (atoms g^{-1} yr^{-1})	f_{10}^* (dimensionless)	$f_3^* f_C f_D$ (dimensionless)
Zero-erosion end-member	1.18	–	142.4	2.82	0.00534	0.05783
Steady-erosion end-member	–	41.1	143.9	3.36	0.00183	0.00337

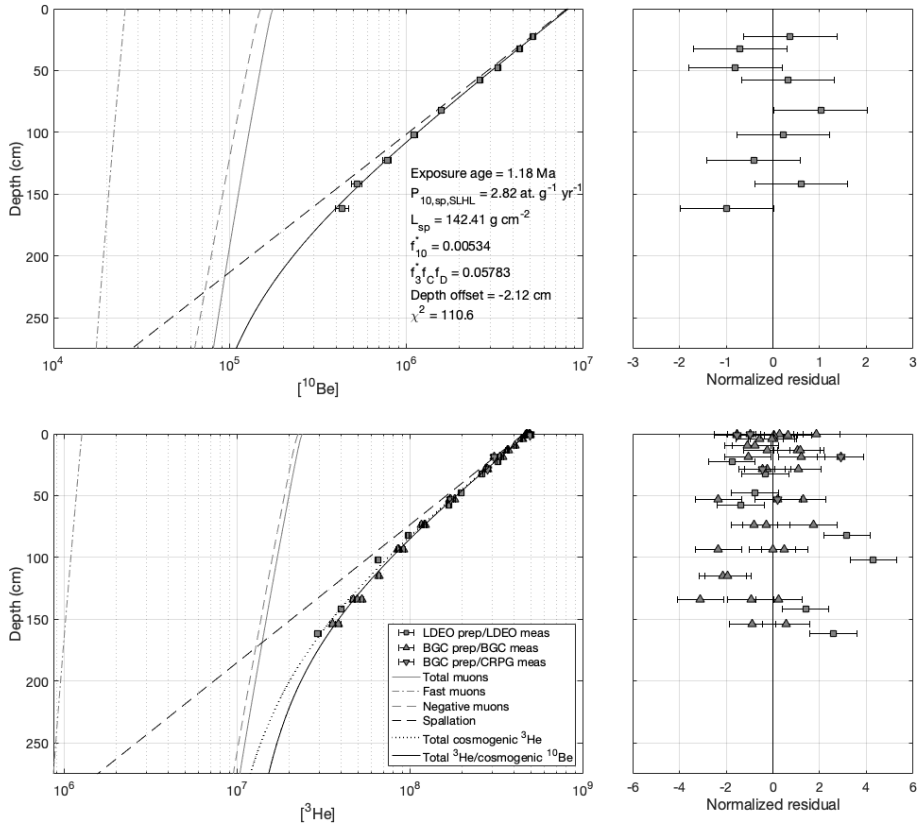

Figure 5. Model results for Labyrinth core under the zero-erosion assumption. Optimal values for parameters are shown in the text inset in the top left panel.

imum value $M = 111$ for 24 degrees of freedom (reduced $\chi^2 = 4.6$).

Figure 6 gives the results of the steady-erosion exercise. The optimal erosion rate over 14.5 Myr is 41.1 cm Myr^{-1}, which agrees with the steady-state erosion rate calculated using the measured ^{3}He concentration at the surface (Sect. 4.1). Under the steady-erosion assumption, the best-fitting $P_{10,sp,SLHL}$ is 3.36 atoms g^{-1} yr^{-1}, and the optimal Λsp is 144 g cm^{-2}. Here, the estimate for $P_{10,sp,SLHL}$ is an upper limit. Notably, the optimal $P_{10,sp,SLHL}$ is close to the estimate of Eaves et al. (2018). The best-fitting value for the depth measurement offset below 18 is 2.05 cm.

The optimal values for parameters related to negative-muon capture for the steady-erosion assumption are $f_{10}^* = 0.00183$ and $f_3^* f_C f_D = 0.00337$. Here, the value for f_{10}^* is nearly identical to f_{10}^* for quartz (0.00191; Balco, 2017). In this scenario, however, the optimal $f_3^* f_C f_D$ is also the same magnitude as the expected value from standard rock (Nesterenok and Yakubovich, 2016). The fitted values for $P_{10,sp,SLHL}$, f_{10}^*, and $f_3^* f_C f_D$ for the steady-erosion end-member are closer to the expected values than for the zero-erosion end-member, and there is no geomorphic evidence against steady erosion taking place at the Labyrinth core site. Therefore, going forward, we assume steady erosion for the Labyrinth core and use the muon cross-sections derived under this assumption for calculating muon production rates.

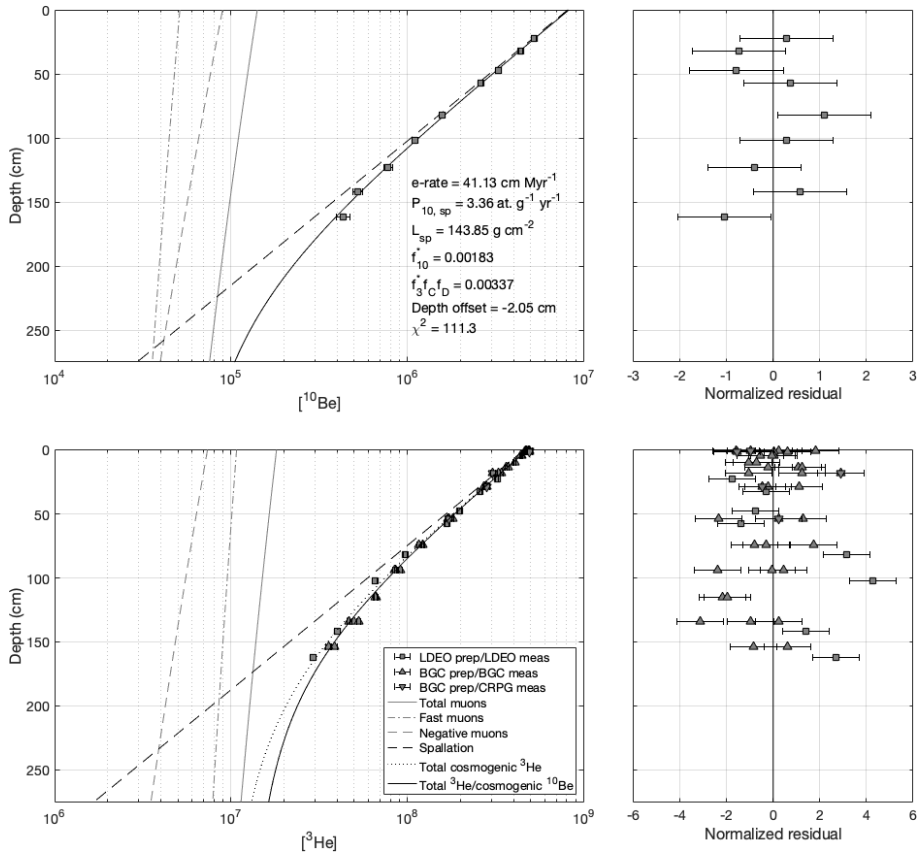

Figure 6. Model results for Labyrinth core for the steady-erosion case. Optimal parameter values are shown in the text inset in the top left panel.

5.1.2 Spallation production in the surface samples

Here, we derive upper and lower limits on the spallation production rate of ^{10}Be in pyroxene using the ^{10}Be and ^{3}He concentrations of the six surface samples by again imposing the zero-erosion (lower limit) and steady-erosion (upper limit) end-members described in Sect. 5.1.1. All calculations of the muon production rates are made using the "Model 1A" MATLAB code of Balco (2017), with the parameter α set to 1 (Balco, 2017; Borchers et al., 2016), the fast-muon-reaction cross-sections described in Sect. 5.1.1, and the negative-muon-capture cross-sections resulting from the steady-erosion end-member for the Labyrinth core.

For the zero-erosion case, we solve the equation

$$P_{10,sp,SLHL,min} = \lambda_{10} \times \frac{(N_{10,m} - N_{10,\mu})}{S_{thick} \times S_{St} \times (1 - e^{-\lambda_{10} t})} \quad (12)$$

for each sample. Here, t is the ^{3}He apparent exposure age,

$$t = \frac{(N_{3,m} - N_{3,non\text{-}cosmo})}{(P_{3,sp,SLHL} \times S_{thick} \times S_{St}) + P_{3,\mu}}, \quad (13)$$

where S_{thick} is the sample thickness correction (dimensionless), and $P_{3,\mu}$ is the total production rate by muons. For the sake of simplicity, we assume that the muon production rate at the center of the sample (sample thickness / 2) is equivalent to $P_{3,\mu}$ in the sample (Balco et al., 2008). We then calculate $N_{10,\mu}$ by evaluating Eqs. (7) and (9) using the "Model 1A" MATLAB code for exposure duration t.

For the steady-erosion case, we assume that each surface has reached saturation with respect to spallation production and decay. To find the maximum $P_{10,sp,SLHL}$ we solve the equation

$$P_{10,sp,SLHL,max} = (N_{10,m} - N_{10,\mu}) \times \frac{(\lambda_{10} + \frac{\varepsilon}{\Lambda sp})}{S_{thick} \times S_{St}} \quad (14)$$

for each sample. Here, the steady erosion rate ε is estimated for each sample by inverting our measured ^{3}He concentrations using a forward model comprising Eqs. (1), (4), (6), and (8) and an exposure duration of 14.5 Myr. We again calculate the muon production rate at the sample midpoint and set $\Lambda sp = 140$ so that the only free parameter in the model is the erosion rate. We fit the model by minimizing the misfit statistic,

$$M = \left[\frac{N_{3,p} - N_{3,m}}{\sqrt{\sigma^2_{3,m} + \sigma^2_{3,non\text{-}cosmo}}} \right]^2. \quad (15)$$

The optimal erosion rate is then used in Eq. (14) to solve for the upper limit on the ^{10}Be spallation production rate.

Together, the zero-erosion and steady-erosion cases yield an allowable range for $P_{10,sp,SLHL}$ given the measured cosmogenic-nuclide concentrations in each surface sample. We take the uncertainty in each value to be the ^{3}He measurement error, ^{10}Be measurement error, and the error in the ^{3}He production rate (11 %) propagated in quadrature.

Figure 7 shows the resulting limits for $P_{10,sp,SLHL}$. The minimum values from the zero-erosion end-member range from 3.2–3.7 atoms g^{-1} yr^{-1}, and the maximum values from the steady-erosion end-member range from 3.9–4.8 atoms g^{-1} yr^{-1}. The overall production rate range encompassed by the surface samples (3.2–4.8 atoms g^{-1} yr^{-1}) overlaps with the limits from the Labyrinth core (2.8–3.4 atoms g^{-1} yr^{-1}).

5.1.3 Spallation production rate for ^{10}Be in pyroxene

Now we combine the complementary information derived from the six surface samples and the Labyrinth core to define a summary distribution for $P_{10,sp,SLHL}$ in pyroxene. The true value for $P_{10,sp,SLHL}$ should fall somewhere between the highest of the lower limits and the lowest of the upper limits of the whole dataset. Therefore, we assume that there is a uniform probability for all production rate values that fall between these limits. To derive a summary distribution using this assumption, we perform a Monte Carlo simulation with 1E+05 iterations. Our summary distribution is described as

$$\sum_{i=1}^{n} \frac{f_i(x)}{\sum f_i(x)}, \text{ where}$$

$$f_i(x) = \begin{cases} 1, & \max\left\{P_{10,\,sp,min,1} \ldots P_{10,\,sp,min,\,j}\right\} < x \\ & < \min\left\{P_{10,\,sp,max,1} \ldots P_{10,\,sp,max,\,j}\right\} \\ 0, & x < \max\left\{P_{10,\,sp,min,1} \ldots P_{10,\,sp,min,\,j}\right\} \\ & \text{or } x > \min\left\{P_{10,\,sp,max,1} \ldots P_{10,\,sp,max,j}\right\}. \end{cases}$$

Here, x is any potential value for the ^{10}Be production rate. $P_{10,sp,min}$ and $P_{10,sp,max}$ are lower and upper limits, respectively, on the ^{10}Be production rate for sample j. For each Monte Carlo iteration n, $P_{10,sp,min}$ and $P_{10,sp,max}$ are randomly drawn from a normal distribution, with the mean and standard deviation of these values found in Sect. 5.1.1 and 5.1.2.

Figure 7 shows the resulting summary distribution. The distribution is approximately Gaussian, with a mean of 3.6 and a standard deviation of 0.2. Therefore, the likely value for the ^{10}Be spallation production rate in pyroxene from our dataset is 3.6 ± 0.2 atoms g^{-1} yr^{-1}. This agrees with the value of 3.6 ± 0.8 atoms g^{-1} yr^{-1}, cross-calibrated with ^{3}He for samples from the mid-latitudes (Eaves et al., 2018), but offers an improvement in the relative uncertainty in this value from ∼ 20 % to ∼ 5 %.

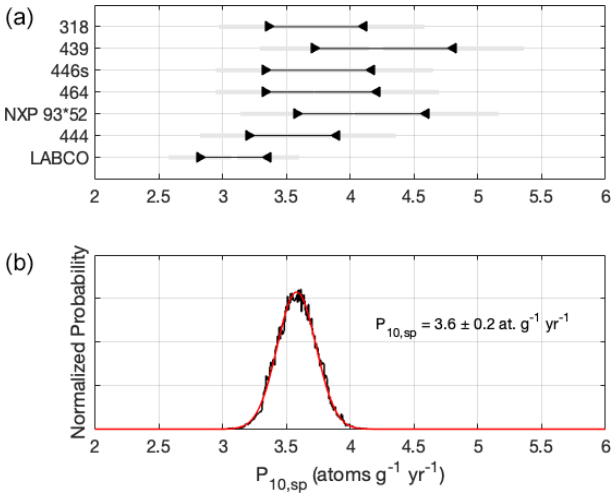

Figure 7. Spallation production rate for ^{10}Be in Ferrar dolerite pyroxene. **(a)** Minimum and maximum values for $P_{10,sp}$. Gray lines show uncertainty in each value. **(b)** Summary distribution of $P_{10,sp}$. The black line shows results from the Monte Carlo simulation described in Sect. 5.1.3. The red line shows the Gaussian distribution constructed using the mean and standard deviation from the Monte Carlo results. The text shows the most likely value for $P_{10,sp}$ given the summary distribution.

5.2 Applications for ^{10}Be in pyroxene

Based on the presented spallation production rate of 3.6 ± 0.2 atoms g^{-1} yr^{-1}, we now explore the potential of ^{10}Be in pyroxene for quantifying ice-sheet and landscape change. On 10^{6}-year timescales, the relative precision of ^{10}Be in pyroxene (∼ 2 %) allows for simultaneously resolving exposure ages and erosion rates using the ^{10}Be–^{3}He pair. Figure 8 shows a ^{10}Be–^{3}He two-nuclide diagram (e.g., Nishiizumi et al., 1991), constructed using our estimate for the spallation ^{10}Be production rate in pyroxene. Our sample concentrations are located in distinct positions throughout the two-nuclide diagram, generally between the constant-exposure and steady-erosion lines, meaning that our samples have experienced a range of erosion rate–exposure duration combinations. With ^{3}He alone, we found apparent (minimum) exposure ages of ∼ 1–6 Myr for the surface samples. Including ^{10}Be shows that those data are better explained with ∼ 2–8 Myr of exposure at erosion rates of ∼ 0–35 cm Myr^{-1}, highlighting the power of this novel two-nuclide approach in pyroxene.

Canonically, the Dry Valleys landscape formed ∼ 14.5 Myr ago and has been preserved by extremely low erosion rates since that time (e.g., Denton and Sugden, 2005; Lewis et al., 2006; Sect. 2). Yet, the oldest surface in our dataset is ∼ 8 Myr when considering erosion, with samples 444 and 439 having exposure ages closer to ∼ 2 Myr (except for the Labyrinth core, which we assume has been exposed for 14.5 Myr under steady erosion for the production rate cal-

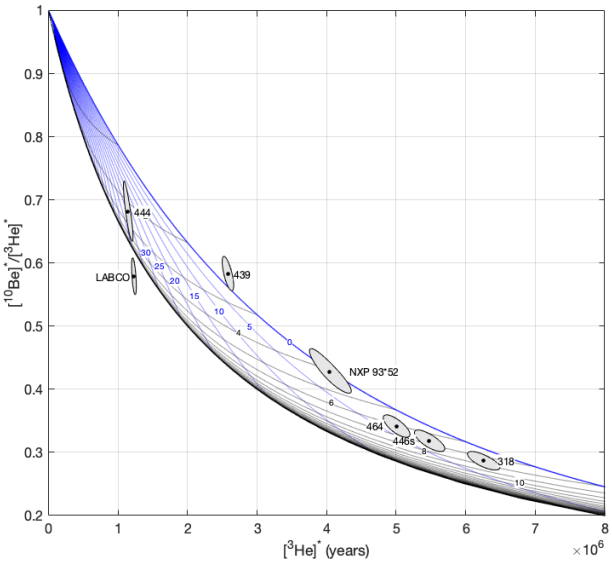

Figure 8. ^{10}Be–^{3}He two-nuclide diagram. Asterisks indicate that nuclide concentrations have been normalized using site-specific production rates for each sample for ease of comparison across sampling locations. The x axis therefore represents apparent ^{3}He years. Production by muons is not included, as a steady-erosion line that includes muons changes with elevation. Ellipses show 68 % confidence intervals based on measurement uncertainties. The ^{10}Be concentration for the Labyrinth core surface (LABCO) sample is taken from the modeled surface concentration under the steady-erosion assumption for the Labyrinth core (Fig. 6) with a conservative 3 % uncertainty. Note that the LABCO concentrations would fall near a steady-erosion line drawn with muons included for elevation of the Labyrinth core, as the ^{10}Be concentration was derived from the modeled steady-state-erosion end-member with 14.5 Myr of exposure. The top line (blue) bounding the steady-erosion island is the simple exposure line, and the bottom bounding line (black) is the steady-erosion line. Blue lines are lines of constant erosion, and black lines are lines of constant age. The diagram shows that measured ^{10}Be and ^{3}He concentrations in the surface samples are consistent with ∼ 2–8 Myr of exposure and ∼ 0–35 cm Myr^{-1} of erosion.

ibration; Sect. 5.1.1). Although our dataset is limited, the fact that several samples have cosmogenic-nuclide concentrations inconsistent with 14.5 Myr of exposure may suggest that the Dry Valleys landscape is more dynamic than once hypothesized, involving either subaerial erosion, burial by ice, or both (Middleton et al., 2012). Applying the ^{10}Be–^{3}He pair in the Dry Valleys and across Antarctica, where much of the exposed rock is mafic Ferrar dolerite, will yield more accurate exposure histories for understanding ice-sheet and landscape change.

In addition to multi-nuclide applications, an obvious use of ^{10}Be in pyroxene is surface exposure dating. At the sample sizes used in this study (0.1–0.2 g pyroxene), ^{10}Be in pyroxene is an ideal exposure chronometer in landscapes like the Dry Valleys, where, owing to long exposure durations at low erosion rates, ^{10}Be concentrations are high (∼ 10^6–10^7 atoms g^{-1}). Applying ^{10}Be in pyroxene for younger landscapes, however, would require increasing the sample size. Eaves et al. (2018) successfully extracted beryllium from 1–2 g of pyroxene using larger resin volumes for cation exchange chromatography than we used here, so an increase to 2 g (or more) of pyroxene is likely possible by combining our pH 8 precipitation step with slightly larger cation resin volumes. Using the relative uncertainties associated with our reported ^{10}Be concentrations (Table S4, Sect. 3.2.3) and assuming 2 g to be a plausible larger sample size, we can estimate the relative uncertainties related to different exposure durations. To achieve relative uncertainties of ∼ 5 %, we would need to measure ∼ 1.2×10^5 atoms of ^{10}Be (Fig. 9). At a sample size of 2 g, this equates to 6×10^4 atoms g^{-1}, or ∼ 17 kyr at high-latitude sea level and ∼ 4 kyr at 2000 m elevation at high latitude. A threshold of 15 % uncertainty would require measurement of 3×10^4 atoms of ^{10}Be, or, at 2 g of pyroxene, a ^{10}Be concentration of 1.5×10^4 atoms g^{-1}. This is equal to ∼ 4 kyr at high-latitude sea level or ∼ 1 kyr at 2000 m elevation at high latitude. A prime target area for applying ^{10}Be in pyroxene to evaluate glacier change in the Late Holocene is the high-altitude Tropical Andes, where moraine boulders are derived from pyroxene-bearing lava flows (e.g., Bromley et al., 2011). Using 2 g of pyroxene from moraines at 4000 m elevation in the tropics would yield 5 % uncertainty for exposure ages of 2 kyr and 15 % uncertainty for exposure ages of 500 years. Importantly, the number of ^{10}Be atoms associated with both of these uncertainty thresholds is greater than the average number of ^{10}Be atoms in our blanks (5.7×10^3 ^{10}Be atoms; Table S5; other users will need to evaluate the limits of these methods for exposure dating given the average blank values from their own laboratories). Therefore, a relatively modest increase in the sample size used here would therefore make ^{10}Be exposure dating in pyroxene useful in landscapes with Last Glacial Maximum to Late Holocene exposure ages.

6 Conclusions

We measured ^{10}Be in Ferrar dolerite pyroxenes from the McMurdo Dry Valleys, Antarctica, with apparent ^{3}He exposure ages of 1–6 Myr. To facilitate the beryllium isolation from pyroxene, we added a pH 8 precipitation to remove Ca, Mg, and Na, reducing the cation load prior to ion exchange chromatography. We also found that with ∼ 20 % sample dissolution through HF leaching, ^{10}Be concentrations stabilized, suggesting complete removal of meteoric ^{10}Be, even in our samples with 10^6-year exposure durations. Our ^{10}Be / ^{9}Be ratios ranged from 5×10^{-13} to 4×10^{-15} for samples with ^{10}Be concentrations from 4×10^{-15} to 6×10^{-13} atoms g^{-1}, with relative uncertainties of 2 %–9 %. The average blank contained 5.7×10^3 atoms of ^{10}Be, and blank corrections ranged from < 1 % in the surface sam-

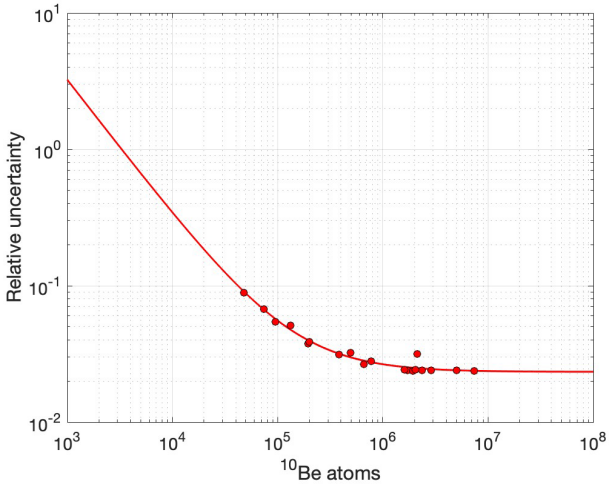

Figure 9. Measured ^{10}Be atoms in pyroxene samples vs. relative uncertainty. The red line is a log-linear fit to the data. From this fit line, it is possible to estimate the relative uncertainty expected when measuring a total number of ^{10}Be atoms.

ples to 7 % at 1.6 m depth in the Labyrinth bedrock core. We derived a ^{10}Be spallation production rate in pyroxene of 3.6 ± 0.2 atoms g^{-1} yr^{-1} using ^{10}Be and ^{3}He concentrations in the six surface samples and the Labyrinth drill core. Our analysis of the Labyrinth core also yields the first direct constraints of the cross-sections for ^{10}Be and ^{3}He production by negative-muon capture ($f^*_{10} = 0.00183$ and $f^*_3 f_C f_D = 0.00337$).

Given the measurement precision, the low-^{10}Be laboratory blanks, and the production rate reported here, ^{10}Be in pyroxene can now be applied for surface exposure dating, burial dating, and erosion quantification. For example, we estimate that surfaces exposed for 2 kyr at 4000 m in the Tropical Andes could be dated with 5 % uncertainty using our beryllium extraction methods for pyroxene. Furthermore, the application of the ^{10}Be–^{3}He pair in pyroxene reveals that our cosmogenic-nuclide concentrations in surface samples located throughout the Antarctic Dry Valleys are consistent with $\sim$ 2–8 Myr of exposure at 0–35 cm Myr^{-1}, offering more insight into the ice-sheet and denudation histories of the Dry Valleys than does ^{3}He alone. With this dataset, we observe that locations throughout the Dry Valleys have a range of exposure and erosional histories. Expanding the use of the ^{10}Be–^{3}He pair beyond surfaces that appear to be stable and to have experienced low erosion will yield further insight into this Antarctic landscape that is likely more dynamic than once hypothesized. In Antarctica and beyond, the ^{10}Be–^{3}He nuclide pair opens new opportunities for more accurately quantifying glacier and landscape histories in mafic rocks.

Code and data availability. All analytical information associated with cosmogenic-nuclide measurements appear in the tables and Supplement. All MATLAB scripts used for model fitting and to generate the figures can be found at https://doi.org/10.5281/zenodo.8125448 (Balter-Kennedy and Balco, 2023).

Supplement. The supplement related to this article is available online at: https://doi.org/10.5194/gchron-5-301-2023-supplement.

Author contributions. ABK, RS, GB, and BT carried out sample preparation. ABK and RS performed beryllium extraction. GB, GW, JL, LP, BT, and PHB performed helium analysis, and beryllium measurements were performed by AJH. ABK and GB performed data analysis. ABK prepared the manuscript with contributions from JMS, GB, RS, GW, JM, JLL, AJH, and PHB.

Competing interests. At least one of the (co-)authors is a member of the editorial board of *Geochronology*. The peer-review process was guided by an independent editor, and the authors also have no other competing interests to declare.

Disclaimer. Publisher's note: Copernicus Publications remains neutral with regard to jurisdictional claims in published maps and institutional affiliations.

Acknowledgements. We would like to acknowledge John Stone for kindly providing samples from the Labyrinth Core. This is LLNL-JRNL-842145, prepared in part by LLNL under contract DE-AC52-07NA27344. We would like to thank Dave Walker for help with calculating the mineral composition of the pyroxene samples.

Financial support. This work is based upon work supported by the National Science Foundation Graduate Research Fellowship under grant no. DGE 2036197 to Allie Balter-Kennedy. Work at LDEO was supported in part by the NSF Office of Polar Programs (award no. 1744895 to Jennifer L. Lamp and Joerg M. Schaefer) and the NSF Division of Behavior and Cognitive Sciences (award no. 1853881 to Joerg M. Schaefer). Joerg M. Schaefer also received support from the Vetlesen Foundation. Work at BGC was supported by the Ann and Gordon Getty Foundation. CRPG funded helium analyses with the ANR JC EroMed (PI PH Blard, 2017-2022).

Review statement. This paper was edited by Yeong Bae Seong and reviewed by Shaun Eaves and Mark Kurz.

References

Ackert, R. P.: Antarctic glacial chronology: new constraints from surface exposure dating, Doctoral thesis, Massachusetts Institute of Technology and Woods Hole Oceanographic Institution, Woods Hole Open Access Server, https://doi.org/10.1575/1912/4123, 2000.

Ackert, R. P. and Kurz, M. D.: Age and uplift rates of Sirius Group sediments in the Dominion Range, Antarctica, from surface exposure dating and geomorphology, Global Planet. Change, 42, 207–225, https://doi.org/10.1016/j.gloplacha.2004.02.001, 2004.

Andrews, J. N. and Kay, R. L. F.: Natural production of tritium in permeable rocks, Nature, 298, 361–363, https://doi.org/10.1038/298361a0, 1982.

Argento, D. C., Stone, J. O., Reedy, R. C., and O'Brien, K.: Physics-based modeling of cosmogenic nuclides part II – Key aspects of in-situ cosmogenic nuclide production, Quat Geochronol, 26, 44–55, https://doi.org/10.1016/j.quageo.2014.09.005, 2015.

Balco, G.: Production rate calculations for cosmic-ray-muon-produced ^{10}Be and ^{26}Al benchmarked against geological calibration data, Quat. Geochronol., 39, 150–173, https://doi.org/10.1016/j.quageo.2017.02.001, 2017.

Balco, G.: Noncosmogenic helium-3 in pyroxene and Antarctic exposure dating: https://cosmognosis.wordpress.com/2020/08/22/noncosmogenic-helium-3-in-pyroxene-and-antarctic-exposure-dating/, last access: 23 June 2022, 2020.

Balco, G. and Shuster, D. L.: ^{26}Al–^{10}Be–^{21}Ne burial dating, Earth Planet. Sc. Lett., 286, 570–575, https://doi.org/10.1016/j.epsl.2009.07.025, 2009.

Balco, G. and Rovey, C. W.: Absolute chronology for major Pleistocene advances of the Laurentide Ice Sheet, Geology, 38, 795–798, https://doi.org/10.1130/g30946.1, 2010.

Balco, G., Stone, J. O., Lifton, N. A., and Dunai, T. J.: A complete and easily accessible means of calculating surface exposure ages or erosion rates from ^{10}Be and ^{26}Al measurements, Quat. Geochronol., 3, 174–195, https://doi.org/10.1016/j.quageo.2007.12.001, 2008.

Balco, G., Blard, P.-H., Shuster, D. L., Stone, J. O. H., and Zimmermann, L.: Cosmogenic and nucleogenic ^{21}Ne in quartz in a 28-meter sandstone core from the McMurdo Dry Valleys, Antarctica, Quat. Geochronol., 52, 63–76, https://doi.org/10.1016/j.quageo.2019.02.006, 2019.

Balter-Kennedy, A. and Balco, G.: Code supporting Cosmogenic ^{10}Be in pyroxene: laboratory progress, production rate systematics, and application of the ^{10}Be–^{3}He nuclide pair in the Antarctic Dry Valleys, Zenodo [code], https://doi.org/10.5281/zenodo.8125448, 2023.

Balter-Kennedy, A., Bromley, G., Balco, G., Thomas, H., and Jackson, M. S.: A 14.5-million-year record of East Antarctic Ice Sheet fluctuations from the central Transantarctic Mountains, constrained with cosmogenic ^{3}Be, ^{10}Be, ^{21}Ne, and ^{26}Al, The Cryosphere, 14, 2647–2672, https://doi.org/10.5194/tc-14-2647-2020, 2020.

Bindschadler, R., Vornberger, P., Fleming, A., Fox, A., Mullins, J., Binnie, D., Paulsen, S. J., Granneman, B., and Gorodetzky, D.: The Landsat Image Mosaic of Antarctica, Remote Sens Environ, 112, 4214–4226, https://doi.org/10.1016/j.rse.2008.07.006, 2008.

Blard, P.-H.: Cosmogenic ^{3}He in terrestrial rocks: A review, Chem. Geol., 586, 120543, https://doi.org/10.1016/j.chemgeo.2021.120543, 2021.

Blard, P.-H., Pik, R., Lavé, J., Bourlès, D., Burnard, P. G., Yokochi, R., Marty, B., and Trusdell, F.: Cosmogenic ^{3}He production rates revisited from evidences of grain size dependent release of matrix-sited helium, Earth Planet. Sc. Lett., 247, 222–234, https://doi.org/10.1016/j.epsl.2006.05.012, 2006.

Blard, P.-H., Bourlès, D., Pik, R., and Lavé, J.: In situ cosmogenic ^{10}Be in olivines and pyroxenes, Quat. Geochronol., 3, 196–205, https://doi.org/10.1016/j.quageo.2007.11.006, 2008.

Blard, P.-H., Balco, G., Burnard, P. G., Farley, K. A., Fenton, C. R., Friedrich, R., Jull, A. J. T., Niedermann, S., Pik, R., Schaefer, J. M., Scott, E. M., Shuster, D. L., Stuart, F. M., Stute, M., Tibari, B., Winckler, G., and Zimmermann, L.: An inter-laboratory comparison of cosmogenic ^{3}He and radiogenic 4He in the CRONUS-P pyroxene standard, Quat. Geochronol., 26, 11–19, https://doi.org/10.1016/j.quageo.2014.08.004, 2015.

Borchers, B., Marrero, S., Balco, G., Caffee, M., Goehring, B., Lifton, N., Nishiizumi, K., Phillips, F., Schaefer, J., and Stone, J.: Geological calibration of spallation production rates in the CRONUS-Earth project, Quat. Geochronol., 31, 188–198, https://doi.org/10.1016/j.quageo.2015.01.009, 2016.

Bromley, G. R. M., Hall, B. L., Schaefer, J. M., Winckler, G., Todd, C. E., and Rademaker, K. M.: Glacier fluctuations in the southern Peruvian Andes during the late-glacial period, constrained with cosmogenic ^{3}He, J. Quat. Sci., 26, 37–43, https://doi.org/10.1002/jqs.1424, 2011.

Bromley, G. R. M., Winckler, G., Schaefer, J. M., Kaplan, M. R., Licht, K. J., and Hall, B. L.: Pyroxene separation by HF leaching and its impact on helium surface-exposure dating, Quat. Geochronol., 23, 1–8, https://doi.org/10.1016/j.quageo.2014.04.003, 2014.

Brown, E. T., Edmond, J. M., Raisbeck, G. M., Yiou, F., Kurz, M. D., and Brook, E. J.: Examination of surface exposure ages of Antarctic moraines using in situ produced ^{10}Be and ^{26}Al, Geochim. Cosmochim. Ac., 55, 2269–2283, https://doi.org/10.1016/0016-7037(91)90103-c, 1991.

Brown, E. T., Brook, E. J., Raisbeck, G. M., Yiou, F., and Kurz, M. D.: Effective attenuation lengths of cosmic rays producing ^{10}Be and ^{26}Al in quartz: Implications for exposure age dating, Geophys. Res. Lett., 19, 369–372, https://doi.org/10.1029/92gl00266, 1992.

Bruno, L. A., Baur, H., Graf, T., Schlüchter, C., Signer, P., and Wieler, R.: Dating of Sirius Group tillites in the Antarctic Dry Valleys with cosmogenic ^{3}He and ^{21}Ne, Earth Planet. Sc. Lett., 147, 37–54, https://doi.org/10.1016/s0012-821x(97)00003-4, 1997.

Burgess, S. D., Bowring, S. A., Fleming, T. H., and Elliot, D. H.: High-precision geochronology links the Ferrar large igneous province with early-Jurassic ocean anoxia and biotic crisis, Earth Planet. Sc. Lett., 415, 90–99, https://doi.org/10.1016/j.epsl.2015.01.037, 2015.

Cerling, T. E.: Dating geomorphologic surfaces using cosmogenic ^{3}He, Quat. Res., 33, 148–156, https://doi.org/10.1016/0033-5894(90)90015-d, 1990.

Cerling, T. E.: Geomorphology and In-Situ Cosmogenic Isotopes, Annu. Rev. Earth Pl. Sc., 22, 273–317, https://doi.org/10.1146/annurev.earth.22.1.273, 1994.

Chmeleff, J., Blanckenburg, F. von, Kossert, K., and Jakob, D.: Determination of the ^{10}Be half-life by multicollector ICP-MS and liquid scintillation counting, Nucl. Instruments Methods Phys. Res. Sect B., 268, 192–199, https://doi.org/10.1016/j.nimb.2009.09.012, 2010.

Denton, G. H. and Sugden, D. E.: Meltwater features that suggest Miocene ice-sheet overriding of the Transantarctic Mountains in Victoria Land, Antarctica, Geogr. Ann, Ser. Phys. Geogr., 87, 67–85, https://doi.org/10.1111/j.0435-3676.2005.00245.x, 2005.

Denton, G. H., Sugden, D. E., Marchant, D. R., Hall, B. L., and Wilch, T. I.: East Antarctic Ice Sheet Sensitivity to Pliocene Climatic Change from a Dry Valleys Perspective, Geogr. Ann, Ser. Phys. Geogr., 75, 155–204, https://doi.org/10.2307/521200, 1993.

Dunai, T. J.: Cosmogenic Nuclides, https://doi.org/10.1017/cbo9780511804519, 2010.

Eaves, S. R., Collins, J. A., Jones, R. S., Norton, K. P., Tims, S. G., and Mackintosh, A. N.: Further constraint of the in situ cosmogenic ^{10}Be production rate in pyroxene and a viability test for late Quaternary exposure dating, Quat. Geochronol., 48, 121–132, https://doi.org/10.1016/j.quageo.2018.09.006, 2018.

Egidy, T. and von and Hartmann, F. J.: Average muonic Coulomb capture probabilities for 65 elements, Phys. Rev. A, 26, 2355–2360, https://doi.org/10.1103/physreva.26.2355, 1982.

Fink, D. and Smith, A.: An inter-comparison of ^{10}Be and ^{26}Al AMS reference standards and the ^{10}Be half-life, Nucl. Instruments Methods Phys. Res. Sect B., 259, 600–609, https://doi.org/10.1016/j.nimb.2007.01.299, 2007.

Gayer, E., Pik, R., Lavé, J., France-Lanord, C., Bourlès, D., and Marty, B.: Cosmogenic ^{3}He in Himalayan garnets indicating an altitude dependence of the ^{3}He / ^{10}Be production ratio, Earth Planet. Sc. Lett., 229, 91–104, https://doi.org/10.1016/j.epsl.2004.10.009, 2004.

Goehring, B. M., Kurz, M. D., Balco, G., Schaefer, J. M., Licciardi, J., and Lifton, N.: A reevaluation of in situ cosmogenic ^{3}He production rates, Quat. Geochronol., 5, 410–418, https://doi.org/10.1016/j.quageo.2010.03.001, 2010.

Gosse, J. C. and Phillips, F. M.: Terrestrial in situ cosmogenic nuclides: theory and application, Quat. Sci. Rev., 20, 1475–1560, https://doi.org/10.1016/s0277-3791(00)00171-2, 2001.

Granger, D. E.: A review of burial dating methods using ^{26}Al and ^{10}Be, in: In Situ-Produced Cosmogenic Nuclides and Quantification of Geological Processes: Geological Society of America Special Paper 415, edited by: Siame, L. L., Bourlès, D. L., and Brown, 1–16, https://doi.org/10.1130/2006.2415(01), 2006.

Heisinger, B., Lal, D., Jull, A. J. T., Kubik, P., Ivy-Ochs, S., Neumaier, S., Knie, K., Lazarev, V., and Nolte, E.: Production of selected cosmogenic radionuclides by muons 1. Fast muons, Earth Planet. Sc. Lett., 200, 345–355, https://doi.org/10.1016/s0012-821x(02)00640-4, 2002a.

Heisinger, B., Lal, D., Jull, A. J. T., Kubik, P., Ivy-Ochs, S., Knie, K., and Nolte, E.: Production of selected cosmogenic radionuclides by muons: 2. Capture of negative muons, Earth Planet. Sc. Lett., 200, 357–369, https://doi.org/10.1016/s0012-821x(02)00641-6, 2002b.

Hippe, K.: Constraining processes of landscape change with combined in situ cosmogenic ^{14}C-^{10}Be analysis, Quat. Sci. Rev., 173, 1–19, https://doi.org/10.1016/j.quascirev.2017.07.020, 2017.

Ivy-Ochs, S., Kubik, P. W., Masarik, J., Wieler, R., Bruno, L., and Schlüchter, C.: Preliminary results on the use of pyroxene for ^{10}Be surface exposure dating, Schweiz, Mineral. Petrogr. Mitt., 78, 375–382, 1998.

Ivy-Ochs, S., Schlüchter, C., Kubik, P. W., Dittrich-Hannen, B., and Beer, J.: Minimum ^{10}Be exposure ages of early Pliocene for the Table Mountain plateau and the Sirius Group at Mount Fleming, Dry Valleys, Antarctica, Geology, 23, 1007–1010, https://doi.org/10.1130/0091-7613(1995)023<1007:mbeaoe>2.3.co;2, 1995.

Kaplan, M. R., Licht, K. J., Winckler, G., Schaefer, J. M., Bader, N., Mathieson, C., Roberts, M., Kassab, C. M., Schwartz, R., and Graly, J. A.: Middle to Late Pleistocene stability of the central East Antarctic Ice Sheet at the head of Law Glacier, Geology, 45, 963–966, https://doi.org/10.1130/g39189.1, 2017.

Kohl, C. P. and Nishiizumi, K.: Chemical isolation of quartz for measurement of in-situ -produced cosmogenic nuclides, Geochim. Cosmochim. Ac., 56, 3583–3587, https://doi.org/10.1016/0016-7037(92)90401-4, 1992.

Kurz, M. D.: Cosmogenic helium in a terrestrial igneous rock, Nature, 320, 435–439, https://doi.org/10.1038/320435a0, 1986.

Kurz, M. D. and Brook, E. J.: Surface exposure dating with cosmogenic nuclides, in: Dating in exposed and surface contexts, 139–159, 1994.

Lal, D.: Production of ^{3}He in terrestrial rocks, Chem Geology Isotope Geosci. Sect., 66, 89–98, https://doi.org/10.1016/0168-9622(87)90031-5, 1987.

Lal, D.: Cosmic ray labeling of erosion surfaces: in situ nuclide production rates and erosion models, Earth Planet. Sc. Lett., 104, 424–439, https://doi.org/10.1016/0012-821x(91)90220-c, 1991.

Lamp, J. L., Marchant, D. R., Mackay, S. L., and Head, J. W.: Thermal stress weathering and the spalling of Antarctic rocks, J. Geophys. Res.-Ea., 122, 3–24, https://doi.org/10.1002/2016jf003992, 2017.

Larsen, I. J., Farley, K. A., Lamb, M. P., and Pritchard, C. J.: Empirical evidence for cosmogenic ^{3}He production by muons, Earth Planet. Sc. Lett., 562, 116825, https://doi.org/10.1016/j.epsl.2021.116825, 2021.

Lewis, A. R., Marchant, D. R., Kowalewski, D. E., Baldwin, S. L., and Webb, L. E.: The age and origin of the Labyrinth, western Dry Valleys, Antarctica: Evidence for extensive middle Miocene subglacial floods and freshwater discharge to the Southern Ocean, Geology, 34, 513–516, https://doi.org/10.1130/g22145.1, 2006.

Margerison, H. R., Phillips, W. M., Stuart, F. M., and Sugden, D. E.: Cosmogenic ^{3}He concentrations in ancient flood deposits from the Coombs Hills, northern Dry Valleys, East Antarctica: interpreting exposure ages and erosion rates, Earth Planet. Sc. Lett., 230, 163–175, https://doi.org/10.1016/j.epsl.2004.11.007, 2005.

Matsuda, J., Matsumoto, T., Sumino, H., Nagao, K., Yamamoto, J., Miura, Y., Kaneoka, I., Takahata, N., and Sano, Y.: The ^{3}He / ^{4}He ratio of the new internal He Standard of Japan (HESJ), Geochem J., 36, 191–195, https://doi.org/10.2343/geochemj.36.191, 2002.

Matsuoka, K., Skoglund, A., Roth, G., Pomereu, J. de, Griffiths, H., Headland, R., Herried, B., Katsumata, K., Brocq, A. L., Licht, K., Morgan, F., Neff, P. D., Ritz, C., Scheinert, M., Tamura, T., Putte, A. V. de, Broeke, M. van den, Deschwanden, A. von, Deschamps-Berger, C., Liefferinge, B.

V., Tronstad, S., and Melvær, Y.: Quantarctica, an integrated mapping environment for Antarctica, the Southern Ocean, and sub-Antarctic islands, Environ Model. Softw., 140, 105015, https://doi.org/10.1016/j.envsoft.2021.105015, 2021.

McKelvey, B. C. and Webb, P. N.: Geological investigations in southern Victoria Land, Antarctica, New Zeal J. Geol. Geop., 5, 143–162, https://doi.org/10.1080/00288306.1962.10420116, 1962.

Middleton, J. L., Ackert, R. P., and Mukhopadhyay, S.: Pothole and channel system formation in the McMurdo Dry Valleys of Antarctica: New insights from cosmogenic nuclides, Earth Planet. Sc. Lett., 355, 341–350, https://doi.org/10.1016/j.epsl.2012.08.017, 2012.

Nespolo, M.: Reference Module in Earth Systems and Environmental Sciences, Encyclopedia of Geology, 2nd Edn., 287–296, https://doi.org/10.1016/b978-0-12-409548-9.12409-1, 2020.

Nesterenok, A. V. and Yakubovich, O. V.: Production of ^{3}He in Rocks by Reactions Induced by Particles of the Nuclear-Active and Muon Components of Cosmic Rays: Geological and Petrological Implications, Arxiv, https://doi.org/10.48550/arxiv.1607.08770, 2016.

Niedermann, S., Schaefer, J. M., Wieler, R., and Naumann, R.: The production rate of cosmogenic ^{38}Ar from calcium in terrestrial pyroxene, Earth Planet. Sc. Lett., 257, 596–608, https://doi.org/10.1016/j.epsl.2007.03.020, 2007.

Nishiizumi, K., Imamura, M., Caffee, M. W., Southon, J. R., Finkel, R. C., and McAninch, J.: Absolute calibration of ^{10}Be AMS standards, Nucl. Instruments Methods Phys. Res. Sect. B., 258, 403–413, https://doi.org/10.1016/j.nimb.2007.01.297, 2007.

Nishiizumi, K., Klein, J., Middleton, R., and Craig, H.: Cosmogenic^{10}Be, ^{26}Al, and ^{3}He in olivine from Maui lavas, Earth Planet. Sc. Lett., 98, 263–266, https://doi.org/10.1016/0012-821x(90)90028-v, 1990.

Nishiizumi, K., Kohl, C. P., Arnold, J. R., Klein, J., Fink, D., and Middleton, R.: Cosmic ray produced ^{10}Be and ^{26}Al in Antarctic rocks: exposure and erosion history, Earth Planet. Sc. Lett., 104, 440–454, https://doi.org/10.1016/0012-821x(91)90221-3, 1991.

Ochs, M. and Ivy-Ochs, S.: The chemical behavior of Be, Al, Fe, Ca and Mg during AMS target preparation from terrestrial silicates modeled with chemical speciation calculations, Nucl. Instruments Methods Phys. Res. Sect. B., 123, 235–240, https://doi.org/10.1016/s0168-583x(96)00680-5, 1997.

Schäfer, J. M., Ivy-Ochs, S., Wieler, R., Leya, I., Baur, H., Denton, G. H., and Schlüchter, C.: Cosmogenic noble gas studies in the oldest landscape on earth: surface exposure ages of the Dry Valleys, Antarctica, Earth Planet. Sc. Lett., 167, 215–226, https://doi.org/10.1016/s0012-821x(99)00029-1, 1999.

Schaefer, J. M., Faestermann, T., Herzog, G. F., Knie, K., Korschinek, G., Masarik, J., Meier, A., Poutivtsev, M., Rugel, G., Schlüchter, C., Serifiddin, F., and Winckler, G.: Terrestrial manganese-53 – A new monitor of Earth surface processes, Earth Planet. Sc. Lett., 251, 334–345, https://doi.org/10.1016/j.epsl.2006.09.016, 2006.

Schaefer, J. M., Denton, G. H., Kaplan, M., Putnam, A., Finkel, R. C., Barrell, D. J. A., Andersen, B. G., Schwartz, R., Mackintosh, A., Chinn, T., and Schlüchter, C.: High-Frequency Holocene Glacier Fluctuations in New Zealand Differ from the Northern Signature, Science, 324, 622–625, https://doi.org/10.1126/science.1169312, 2009.

Schaefer, J. M., Finkel, R. C., Balco, G., Alley, R. B., Caffee, M. W., Briner, J. P., Young, N. E., Gow, A. J., and Schwartz, R.: Greenland was nearly ice-free for extended periods during the Pleistocene, Nature, 540, 252–255, https://doi.org/10.1038/nature20146, 2016a.

Schaefer, J. M., Winckler, G., Blard, P.-H., Balco, G., Shuster, D. L., Friedrich, R., Jull, A. J. T., Wieler, R., and Schluechter, C.: Performance of CRONUS-P – A pyroxene reference material for helium isotope analysis, Quat. Geochronol., 31, 237–239, https://doi.org/10.1016/j.quageo.2014.07.006, 2016b.

Schaefer, J. M., Codilean, A. T., Willenbring, J. K., Lu, Z.-T., Keisling, B., Fülöp, R.-H., and Val, P.: Cosmogenic nuclide techniques, Nat. Rev. Meth. Prim., 2, 18, https://doi.org/10.1038/s43586-022-00096-9, 2022.

Stone, J. O.: Air pressure and cosmogenic isotope production, J. Geophys. Res. Sol.-Ea., 105, 23753–23759, https://doi.org/10.1029/2000jb900181, 2000.

Sugden, D. E., Marchant, D. R., Potter, N., Souchez, R. A., Denton, G. H., III, C. C. S., and Tison, J.-L.: Preservation of Miocene glacier ice in East Antarctica, Nature, 376, 412–414, https://doi.org/10.1038/376412a0, 1995.

Summerfield, M. A., Stuart, F. M., Cockburn, H. A. P., Sugden, D. E., Denton, G. H., Dunai, T., and Marchant, D. R.: Long-term rates of denudation in the Dry Valleys, Transantarctic Mountains, southern Victoria Land, Antarctica based on in-situ-produced cosmogenic ^{21}Ne, Geomorphology, 27, 113–129, https://doi.org/10.1016/s0169-555x(98)00093-2, 1999.

Young, N. E., Lesnek, A. J., Cuzzone, J. K., Briner, J. P., Badgeley, J. A., Balter-Kennedy, A., Graham, B. L., Cluett, A., Lamp, J. L., Schwartz, R., Tuna, T., Bard, E., Caffee, M. W., Zimmerman, S. R. H., and Schaefer, J. M.: In situ cosmogenic ^{10}Be–^{14}C–^{26}Al measurements from recently deglaciated bedrock as a new tool to decipher changes in Greenland Ice Sheet size, Clim. Past, 17, 419–450, https://doi.org/10.5194/cp-17-419-2021, 2021.

Zavala, K., Leitch, A. M., and Fisher, G. W.: Silicic Segregations of the Ferrar Dolerite Sills, Antarctica, J. Petrol., 52, 1927–1964, https://doi.org/10.1093/petrology/egr035, 2011.

Zimmermann, L., Avice, G., Blard, P.-H., Marty, B., Füri, E., and Burnard, P. G.: A new all-metal induction furnace for noble gas extraction, Chem. Geol., 480, 86–92, https://doi.org/10.1016/j.chemgeo.2017.09.018, 2018.